

Development of a Muon Polarimeter  
for  
the J-PARC T-violation search experiment

Master's thesis

Aine Kobayashi

35-116038  
Department of Physics  
Graduate School of Science, University of Tokyo

January 7th 2013



## Abstract

This thesis reports the performance evaluation of a muon tube polarimeter for the J-PARC E06 (TREK) experiment which aims to measure T violation via a measurement of the transverse muon polarization in  $K^+ \rightarrow \pi^0 \mu^+ \nu$  decay.



# Contents

<b>1</b>	<b>Introduction</b>	<b>1</b>
<b>2</b>	<b>Physics motivations</b>	<b>3</b>
2.1	Matter and antimatter asymmetry . . . . .	3
2.2	C,P,CP violation . . . . .	4
2.3	T-violation search experiments . . . . .	4
<b>3</b>	<b>J-PARC TREK</b>	<b>5</b>
3.1	Phenomenology of $K_{\mu 3}^+$ decay . . . . .	5
3.2	Transverse Polarization $P_T$ . . . . .	7
3.3	Theoretical Predictions . . . . .	9
3.3.1	Standard Model . . . . .	9
3.3.2	Final state interactions . . . . .	9
3.3.3	Multi-Higgs doublet model . . . . .	10
3.3.4	SUSY models . . . . .	11
3.4	J-PARC TREK Experiment . . . . .	12
3.4.1	Experiment design . . . . .	13
<b>4</b>	<b>Polarimeter</b>	<b>15</b>
4.1	Muon polarimeter . . . . .	15
4.1.1	Principle . . . . .	15
4.1.2	Passive polarimeter for E246 . . . . .	16
4.1.3	The analysis method of the E246 polarimeter . . . . .	16
4.1.4	Requirements for the active polarimeter . . . . .	18
4.1.5	Expected performance of the polarimeter . . . . .	20
4.2	Plate type polarimeter . . . . .	20
4.3	Muon Tube Polarimeter - MTP - . . . . .	22
4.3.1	Drift tube . . . . .	25
4.4	Muon polarimeter magnet . . . . .	26
4.5	Systematic errors . . . . .	27

<b>5</b>	<b>Beam Test at TRIUMF</b>	<b>29</b>
5.1	TRIUMF M11 beam line . . . . .	29
5.2	Preparation . . . . .	31
5.2.1	Preparation . . . . .	31
5.2.2	Beam tuning . . . . .	32
5.2.3	Experimental setup . . . . .	33
5.3	Measurements . . . . .	39
5.4	$\mu$ SR measutement . . . . .	39
<b>6</b>	<b>Data Analysis</b>	<b>45</b>
6.1	Basic Analysis . . . . .	45
6.1.1	Data quality . . . . .	45
6.1.2	Wire efficiency . . . . .	46
6.2	Drift time . . . . .	48
6.3	Tracking . . . . .	52
6.3.1	Event selection . . . . .	52
6.3.2	Tracking algorithm . . . . .	52
6.4	Asymmetry . . . . .	56
6.4.1	Muon decay parameters . . . . .	56
6.4.2	Result of asymmetry measurement by the MTP . . . . .	57
6.4.3	Systematics . . . . .	60
6.4.4	Muon incident angle . . . . .	67
6.5	Analyzing Power . . . . .	67
6.6	More detailed analysis . . . . .	69
<b>7</b>	<b>Conclusion</b>	<b>71</b>
	<b>Appendix A Beam tuing at J-PARC K1.1BR</b>	<b>A-1</b>
	<b>Appendix B Charge division</b>	<b>B-1</b>
	<b>Appendix C Tracking system for the TREK detector</b>	<b>C-1</b>
	<b>Appendix D Read-out system for the polarimeter beam tests</b>	<b>D-1</b>
	<b>Acknowledgements</b>	<b>D-0</b>

# List of Figures

1.1	TREK sensitivity . . . . .	2
3.1	The intensity distribution (a), and the three components of the muon polarizations (b) the longitudinal component $P_L$ , (c) the normal component $P_N$ , and (d) the transverse component $P_T/\text{Im}\xi$ . . . . .	6
3.2	$K_{\mu 3}$ decay . . . . .	7
3.3	Radiative corrections in the $K_{\mu 3}$ decay . . . . .	9
3.4	(a) One of the diagrams of the final state interactions contributing to $P_T^{em}$ ; from one photon exchange calculated in Ref. [1] and also (b) one of the diagrams from two photon exchanges calculated in Ref. [2]. . . . .	10
3.5	End and side views of the TREK deector sysmtem . . . . .	14
4.1	$K_{\mu 3}$ decay and Michel $\mu$ decay, showing helicity conservation . . . . .	15
4.2	Incident muon $y$ distribution in the stopper measured by the C4 chamber (top), and the intrinsic geometrical asymmetry for those muons (bottom). . . . .	17
4.3	Comparison between passive and active polarimeter . . . . .	20
4.4	Muon stopper made of parallel plates which serve also as drift chamber cell structure . . . . .	21
4.5	MTP (size: 865mm $\times$ 284mm $\times$ 330mm, 75kg) . . . . .	23
4.6	MTP YZ-plane . . . . .	23
4.7	Schematic end view of the MTP . . . . .	24
4.8	Time development of an avalanche in a proportional counter. [3] . . . . .	26
4.9	Schematic front view of the muon field magnet . . . . .	27
5.1	Layout of M11 beam channel . . . . .	30
5.2	HV curve . . . . .	31
5.3	Setup for beam tuning and degrader tuning . . . . .	32
5.4	TOF spectrum at 170 MeV/c . . . . .	33
5.5	Timing chart . . . . .	34
5.6	Typical chamber signal . . . . .	34
5.7	Configulation of the DAQ system . . . . .	35
5.8	Gap between CP signals . . . . .	35

5.9	Degrader tuning ; Telescope (E1 and E2 counters) was placed on MTP . . . . .	36
5.10	Results of the degrader tuning for $\pi$ . . . . .	37
5.11	Results of the degrader tuning for $\mu$ . . . . .	37
5.12	Muon decay curve: The parameter $(1/\tau)$ corresponds to $2.2\mu s$ . . . . .	38
5.13	The confirmation of muon stopping area in MTP. The colored points means wire positions and all of the 256 channels worked well. . . . .	38
5.14	Schematic view of charge division study set up . . . . .	39
5.15	Fiber scintillator for charge division study to define the incident position with a good precision . . . . .	40
5.16	Set up for $\mu SR$ measurement . . . . .	41
5.17	Al sample (5 cm $\times$ 2.4 cm $\times$ 2 cm ) . . . . .	42
5.18	S3 counter timing spectrum : Muon stopping timing (the spike at $\sim 2500$ ) and the oscillation pattern are seen. . . . .	42
5.19	Fitting result of the $\mu SR$ oscillation spectrum . . . . .	43
5.20	Calibrated time spectrum of the S3 signals. . . . .	44
6.1	The S2 counter time spectrum. The S2 counter was used for determining the TDC stop timing. . . . .	45
6.2	Wire efficiency . . . . .	46
6.3	Efficiency as a function of the drift distance . . . . .	47
6.4	Schematic view of the wire efficiency of z-direction; the wire efficiency is expressed as (the middle of the A wire hit)/(all of the A, B, C wires are hit) . . . . .	47
6.5	Drift time distribution . . . . .	48
6.6	Fit to the drift time distribution . . . . .	49
6.7	X2 distribution . . . . .	50
6.8	Schematic view of the definition of position for analyzing the X-T relation . . . . .	50
6.9	$X_2(X_1, X_3)$ versus $t_2$ . . . . .	51
6.10	$X_2(X_1, X_3)$ versus $X_2(t_2)$ . . . . .	51
6.11	Schematic view of the track reconstruction . . . . .	53
6.12	Tracking result with weight for the positron . . . . .	54
6.13	Tracking result without weight for the positron . . . . .	54
6.14	Another example of positron tracking . . . . .	55
6.15	Incident muon tracking reconstruction fit . . . . .	55
6.16	Distribution of decay positrons as a function of $\cos \theta$ and x . . . . .	57
6.17	Schematic view of the tracking angle . . . . .	58
6.18	Opening angle distribution . . . . .	59
6.19	Example of bad events: Its opening angle is small, 0.387, because of there were two incident beam partially and the second beam mis-regarded as the positron, so the average of the positron hit was mis-calculated. . . . .	59
6.20	The coordinate system definition . . . . .	60

6.21	Schematic view of the muon decay for positron in the MTP . . . . .	61
6.22	$\cos \psi$ by analytic calculation . . . . .	62
6.23	$\sin \psi$ by analytic calculation . . . . .	62
6.24	$\cos \psi$ generated by Geant4 simulation . . . . .	62
6.25	$\sin \psi$ generated by Geant4 simulation . . . . .	62
6.26	Definition of the fiducial volume. The area in the dashed line means the read-out region. . . . .	63
6.27	$\cos \psi$ distribution of the muon data . . . . .	63
6.28	$\sin \psi$ distribution of the muon data . . . . .	63
6.29	<i>Forward</i> or <i>backward</i> asymmetry of the muon data . . . . .	64
6.30	<i>Up</i> or <i>down</i> asymmetry of the muon data . . . . .	64
6.31	$\cos \psi$ distribution of the pion data . . . . .	64
6.32	$\sin \psi$ distribution of the pion data . . . . .	64
6.33	<i>Forward</i> or <i>backward</i> asymmetry of the pion data . . . . .	65
6.34	<i>Up</i> or <i>down</i> asymmetry of the pion data . . . . .	65
6.35	Definition of the fiducial volume . . . . .	65
6.36	$\cos \psi$ distribution of the muon data with small fiducial volume . . . .	66
6.37	$\sin \psi$ distribution of the muon data with small fiducial volume . . . .	66
6.38	<i>Forward</i> or <i>backward</i> asymmetry of the muon data with small fidu- cial volume . . . . .	66
6.39	<i>Up</i> or <i>down</i> asymmetry of the muon data with small fiducial volume . . . .	66
6.40	$\cos \psi$ distribution of the pion data with small fiducial volume . . . .	66
6.41	$\sin \psi$ distribution of the pion data with small fiducial volume . . . .	66
6.42	<i>Forward</i> or <i>backward</i> asymmetry of the pion data with small fidu- cial volume . . . . .	67
6.43	<i>Up</i> or <i>down</i> asymmetry of the pion data with small fiducial volume . . . .	67
6.44	no cut $\cos \psi$ . . . . .	68
6.45	no cut $\sin \psi$ . . . . .	68
6.46	After cut of $\chi^2/NDF < 20$ $\sin \psi$ distribution . . . . .	68
A.2	Detectors for beam measurement . . . . .	A-2
A.3	$\pi/K$ differential Fitch-type Čerenkov counter . . . . .	A-3
A.4	The layout of K1.1BR beamline . . . . .	A-3
A.5	Results of $K^+/\pi^+$ separation curve using narrow slit . . . . .	A-5
B.:2	The schematic view of charge division system. . . . .	B-1
B.:3	The equivalent electric circuit of the charge division system. . . . .	B-2
C.2	Schematics of the tracking system in the TREK setup ( <i>right</i> ) com- pared with that of the E246 experiment ( <i>left</i> ). . . . .	C-2



# List of Tables

4.1	Comparison between plate type and tube type . . . . .	24
4.2	Detail of MTP spec . . . . .	24
5.1	Comparison between particles . . . . .	44
C.2	Main parameters of the charged particle tracking. . . . .	C-3
D.2	The main functions of ASB . . . . .	D-2
D.3	The specs of VME discriminator board . . . . .	D-2



# Chapter 1

## Introduction

The Standard Model [4] explains very well the behavior of matter and interactions. In 2012, the discovery of the Higgs boson at the Large Hadron Collider (LHC) [5] experiments completed the Standard Model predictions. However, some theoretical consideration point out that the Standard Model is not the ultimate theory and "New Physics" is needed.

For example, in order to explain the asymmetry of matter and antimatter in the universe, C and CP violation are needed. Although today's Kobayashi-Masukawa theory can explain CP violation in the quarks sector, it is inadequate to explain the size of the asymmetry of matter and antimatter (baryon number asymmetry) today. Therefore CP violation beyond the Kobayashi-Masukawa Standard Model theory is required to explain why our universe mainly consists of baryons and not antibaryons [6]. Also in 2005, the neutrino oscillation was observed at the KamLAND experiment [7]. It is an important key to solve the neutrino flux problem.

According to relativistic local-field theory, CPT [8] symmetry is conserved, hence when CP violation exists, T violation also must exist by necessity. Measurement of T violation in the neutral K meson system means a measurement direct CP violation, this is the effective way for discovery of new physics beyond the Standard Model. I have joined the J-PARC E06 (TREK) experiment [9], which aims to perform a precision measurement of direct T violation by means of a measurement of the transverse polarization  $P_T$  in  $K^+ \rightarrow \mu^+ \pi^0 \nu$  ( $K_{\mu 3}$ ) decay.

$P_T$  is defined as the vertical component of the polarization normal to the  $K_{\mu 3}$  decay plane, and this value is superior in terms of following features:

- very small ( $< 10^{-7}$ ) Standard Model prediction
- very small Final State Interaction ( $\sim 10^{-5}$ )

Therefore, measurement of a  $P_T$  value as large as  $10^{-3} \sim 10^{-4}$  is a probe of T violation and we could discover new physics and possibly explain the origin of the

baryon asymmetry. I describe this theory in Chapter 3.

It is necessary to conduct a very high statistical precision experiment due to smallness of  $P_T$ . The KEK-PS E246 experiment [10], which was the TREK predecessor works, obtained  $P_T = -0.0017 \pm 0.00023(\text{stat}) \pm 0.0011(\text{syst})$  [10] as the worlds record, and the result was consistent with no T violation. The largest uncertainty was due to the large ambiguity on the decay positron arising from muon multiple scattering. In the TREK experiment, we will upgrade the E246 detectors to reduce the systematic error. Fig 1.1 shows the TREK sensitivity.

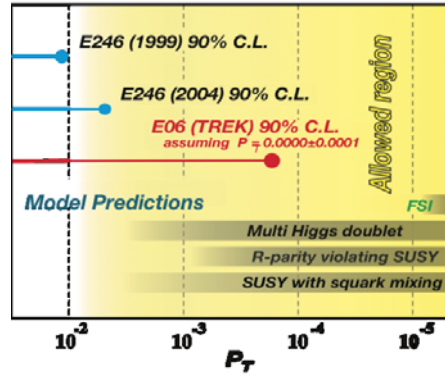


Figure 1.1: TREK sensitivity

In this experiment, I have worked on the research and development of the muon spin polarimeter, which has an important role in the measurement of  $P_T$ . The TREK polarimeter, which I will describe in Chapter 4, stops muons in middle, defines the positron emission angle by tracking both muons and decay positrons. Since the positrons are likely to be emitted to the same direction as the muons due to helicity conservation. Polarimeter has a role not only as a tracker but also as a stopper, so multiple scattering is unavoidable. It's important to make a track reconstruction algorithm to solve this problem for higher accuracy, which I made and describe in Chapter 6.3.

We built a prototype polarimeter and made a beam test at TRIUMF [11] in Oct-Nov 2011. We have done not only the experimental set up such as the arrangement of the polarimeter and the electronic circuit but also TOF particle identification, beam tuning and degrader tuning. I will describe the beam test in Chapter 5, and the data analysis in Chapter 6.

In addition, I joined the beam tuning at J-PARC [12] K1.1BR in June 2012, which is mentioned in the appendix A.

# Chapter 2

## Physics motivations

### 2.1 Matter and antimatter asymmetry

In the very early universe, the symmetry of matter and antimatter was conserved, pair production and pair annihilation always occur [13].

$$\gamma + \gamma \rightleftharpoons q + \bar{q} \quad (2.1)$$

As the temperature of the universe gradually decreased, pair production and pair annihilation slowly decreased. And there must have been processes causing a small matter-antimatter asymmetry, leading to the matter dominant universes of today.

The quantity defined as the matter and antimatter asymmetry is expressed as a ratio of the baryon number density and its entropy density. This ratio remains unchanged under cosmic adiabatic expansion, as long as there is no baryogenesis or entropy production such as reheat. According to the observation value,

$$\frac{n_B}{s/k} = (0.67 - 0.92) \times 10^{-10}. \quad (2.2)$$

Here,  $n_B$  is the baryon number density,  $s$  is the entropy density, and  $k$  is the Boltzmann constant.

This phenomenon can only be explained if the three conditions of Sakharov [6] are fulfilled:

- There must be an interaction violating the conservation of baryon number.
- There must be an interaction violating  $CP$  invariance, where  $C$  is the particle-antiparticle transformation and  $P$  is the space inversion operation.
- There must be phases of the expansion without thermodynamic equilibrium.

The first condition is natural, since there was no baryon asymmetry in early universe, if all of the interactions between particles conserve the baryon number, there should be no baryon asymmetry now. And this criterion would imply that protons are not stable (searches for such a decay have been unsuccessful, showing that the lifetime of the proton is longer than  $10^{33}$  years). However, currently, there is no experimental evidence of the particle interactions, where the conservation of baryon number is broken. The second condition was first shown to be fulfilled by the discovery of the  $CP$  violation in the decay of neutral  $K$  mesons, in 1964, by J.Christenson, J.Cronin, V.Fitch and R.Turlay. The third condition ensures that the reverse process cannot happen with the same probability as the violation of the conservation of baryon number process. This condition can be met in cosmological models by inflationary fast expansion or by a first-order phase transition in the electroweak interaction of the Standard Model [14].

## 2.2 C,P,CP violation

The CPT theorem asserts that a Lorentz-invariant field theory is unchanged under the combined CPT operation, thus conserving CPT. According to the CPT invariance however, the observation of the  $CP$  violation in the  $K^0$  and  $B^0$  systems requires the existence of  $T$  violation. Thus,  $T$  violation has a great impact on our understanding of nature. Before the first observation of indirect  $T$  violation by CPLEAR experiment in 1988 [15], the  $T$ - violation was regarded as kind of statistical fluctuation due to an increase of entropy in our universe. The observation means that the  $T$  violation can be explained as the result of particle interactions.

## 2.3 T-violation search experiments

A large number of experiments to search for  $T$  violating effects have been performed such as the particle and the nuclear electric dipole moment (EDM) experiments [16]. On the other hand, we aim to measure the effect in  $K^+ \rightarrow \pi^0 \mu^+ \nu_\mu (K_{\mu 3})$ . More than 50 years ago, it was suggested by J.Sakurai [17] that the nonzero transverse muon polarization ( $P_T$ ) is a good test for  $T$  violation. The system has several advantages such as the smallness of the final state interactions which can mimic  $T$  violation by inducing a  $T$ -odd effect and the very small Standard Model prediction.

## Chapter 3

# J-PARC TREK

### 3.1 Phenomenology of $K_{\mu 3}^+$ decay

Based on the V-A theory, the decay matrix element can be written as [18], [19]

$$M = \frac{G_F}{2} \sin \theta_C \left[ f_+(q^2) \left( p_K^\lambda + p_\pi^\lambda \right) + f_-(q^2) \left( p_K^\lambda - p_\pi^\lambda \right) \right] \cdot [\bar{u}_\nu \gamma_\lambda (1 - \gamma_5) v_\mu]. \quad (3.1)$$

where,

$G_F$  : the Fermi constant

$\theta_C$  : the Cabibbo angle

$p_K, p_\pi, p_\mu, p_\nu$  : the four-momenta of the kaon, pion, muon and antineutrino

with two form factors  $f_+(q^2)$  and  $f_-(q^2)$  of the momentum transfer squared to the lepton pair,  $q^2 = (p_K - p_\pi)^2$ . Using  $p_K = p_\pi + p_\mu + p_\nu$ , this amplitude can be rewritten as

$$M = \frac{G_F}{2} \sin \theta_C f_+(q^2) \left[ 2p_K^\lambda \cdot \bar{u}_\nu \gamma_\lambda (1 - \gamma_5) v_\mu + (\xi(q^2) - 1) m_\mu \bar{u}_\nu (1 - \gamma_5) v_\mu \right]. \quad (3.2)$$

where the parameter  $\xi(q^2)$  is defined as

$$\xi(q^2) = f_-(q^2)/f_+(q^2). \quad (3.3)$$

The first term of Eq. 3.2 corresponds to the vector and axial vector amplitude, and the second term corresponds to the scalar and pseudoscalar amplitude. The parameters  $f_-$  and  $f_+$  depend on  $q^2$  as

$$f_\pm(q^2) = f_\pm(0) \left[ 1 + \lambda_\pm(q^2/m_\pi^2) \right]. \quad (3.4)$$

In general, both  $f_-$  and  $f_+$  can be complex. If time reversal (T) is a good symmetry, the parameter  $\xi$  is real. Any non-zero value of  $\text{Im}\xi$  would imply T-violation. An experimentally observed T-violating muon polarization  $P_T$  is directly proportional

to  $\text{Im}\xi$ . The currently adopted values are given below;

$$\lambda_+ = 0.0284 \pm 0.0027 \quad (3.5)$$

$$\xi(0) = -0.14 \pm 0.05 \quad (3.6)$$

$$\lambda_- = 0 \quad (3.7)$$

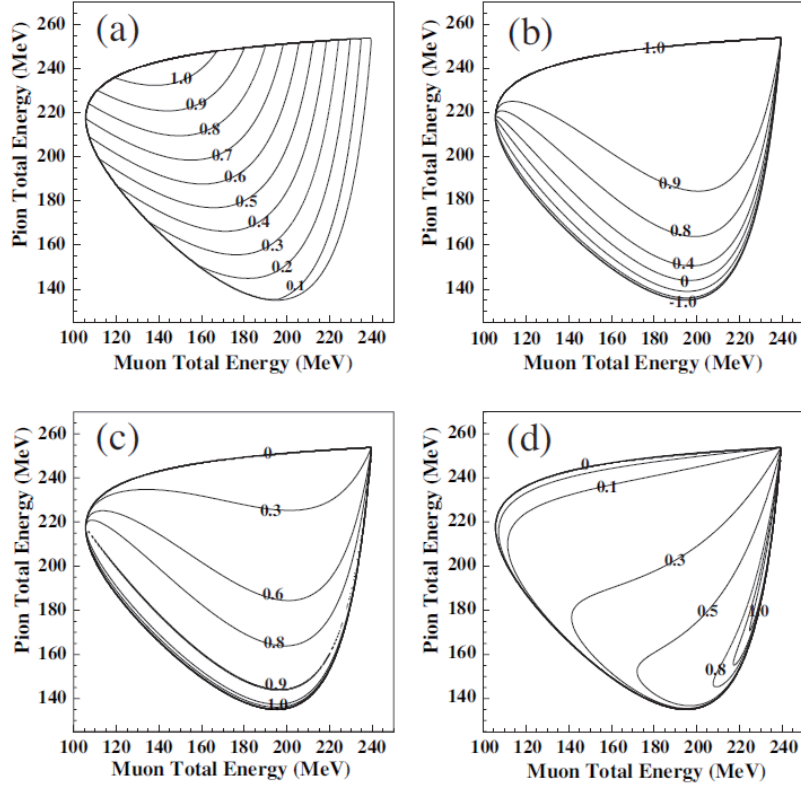


Figure 3.1: The intensity distribution (a), and the three components of the muon polarizations (b) the longitudinal component  $P_L$ , (c) the normal component  $P_N$ , and (d) the transverse component  $P_T/\text{Im}\xi$ .

The Dalitz distribution for  $K_{\mu 3}$  decay is given by Fig 3.1.

$$\rho(E_\pi, E_\mu) \propto f_+^2(q^2) [A + B\xi(q^2) + C\xi^2(q^2)] \quad (3.8)$$

with

$$A = m_K(2E_\mu E_\nu - m_K E'_\pi) + m_\mu^2 \left( \frac{1}{4} E'_\pi - E_\nu \right) \quad (3.9)$$

$$B = m_\mu^2 \left( E_\nu - \frac{1}{2} E'_\pi \right) \quad (3.10)$$

$$C = \frac{1}{4} m_\mu^2 E'_\pi \quad (3.11)$$

$$E'_\pi = (m_K^2 + m_\pi^2 - m_\mu^2)/(2m_K) - E_\pi \quad (3.12)$$

Here,  $E_\pi$ ,  $E_\mu$  and  $E_\nu$  are the energies of the pion, muon and neutrino in the kaon center-of-mass frame, and  $M_K$ ,  $m_\pi$  and  $m_\mu$  the masses of the kaon, pion and muon, respectively.  $M_K$  is the kaon mass. The Dalitz plot is shown in Fig 3.1.

### 3.2 Transverse Polarization $P_T$

In the three body decay, three orthogonal components of the muon polarization vector can be defined: the longitudinal ( $P_L$ ), normal ( $P_N$ ) and transverse ( $P_T$ ) as the components parallel to the muon momentum  $\vec{p}_\mu$ , normal to  $P_L$  in the decay plane, and normal to the decay plane, respectively.

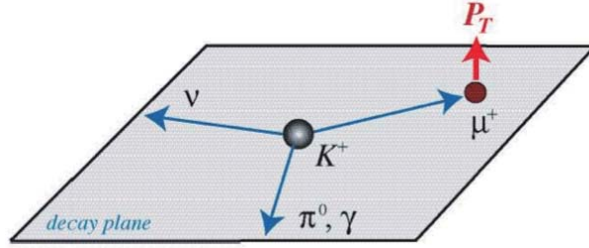


Figure 3.2:  $K_{\mu 3}$  decay

With the polarization vector  $\vec{\sigma}_\mu$ , they are expressed below:

$$P_L = \frac{\vec{\sigma}_\mu \cdot \vec{p}_\nu}{|\vec{p}_\mu|} \quad (3.13)$$

$$P_N = \frac{\vec{\sigma}_\mu \cdot (\vec{p}_\mu \times (\vec{p}_\pi \times \vec{p}_\mu))}{|(\vec{p}_\pi \times \vec{p}_\mu)|} \quad (3.14)$$

$$P_T = \frac{\vec{\sigma}_\mu \cdot (\vec{p}_\pi \times \vec{p}_\mu)}{|\vec{p}_\pi \times \vec{p}_\mu|} \quad (3.15)$$

The  $P_T$  changes sign under the time reversal operation, therefore making it a T-odd observable. With the decay probability, the muon polarization in the kaon rest frame can be written as

$$\vec{\sigma}_\mu = \vec{P}/|\vec{P}|, \quad (3.16)$$

where  $\vec{P}$  is determined as follows

$$\begin{aligned} \vec{P} &= \{a_1(\xi) - a_2(\xi) [(m_K - E_\pi) + (E_\mu - m_\mu)(\vec{p}_\pi \cdot \vec{p}_\mu)/|\vec{p}_\mu|^2]\} \vec{p}_\mu \\ &- a_2(\xi)m_\mu\vec{p}_\pi + m_K m_\mu \text{Im}(\xi)(\vec{p}_\pi \times \vec{p}_\mu). \end{aligned} \quad (3.17)$$

with

$$a_1(\xi) = 2m_K^2 [E_\nu + \text{Re}(b(q^2))(E_\pi^* - E_\pi)], \quad (3.18)$$

$$a_2(\xi) = m_K^2 + 2\text{Re}(b(q^2))m_Ke_\mu + |b(q^2)|^2 m_\mu^2, \quad (3.19)$$

$$b(q^2) = \frac{1}{2} [\xi(q^2) - 1], \text{ and} \quad (3.20)$$

$$E_\pi^* = (m_K^2 + m_\pi^2 - m_\mu^2)/2(m_K). \quad (3.21)$$

These three polarization components are shown in Fig 3.1. In the presence of the predominant in-plane component of the polarizations,  $P_L$  and  $P_N$ ,  $P_T$  (Eq 3.15) can be rewritten in terms of  $\text{Im}\xi$  and a kinematical factor as

$$P_T = \text{Im}\xi \cdot \frac{m_\mu}{m_K} \frac{|\vec{p}_\mu|}{[E_\mu + |\vec{p}_\mu| \vec{n}_\mu \cdot \vec{n}_\nu - m_\mu^2/m_K]}. \quad (3.22)$$

The quantity  $\text{Im}\xi$ , sensitive to T-violation, can be determined from a  $P_T$  measurement. The advantage of  $K_{\mu 3}$  over  $K_{e 3}$  ( $K^+ \rightarrow \pi^0 e^+ \nu$ ) is apparent as  $P_T$  is proportional to the lepton mass. The kinematic factor as a function of the  $\pi^0$  energy ( $2E_{\pi^0}/m_K$ ) and  $\mu^+$  energy ( $2E_{\mu^+}/m_K$ ) is the contour shown in Fig 3.1 which has an average value of  $\sim 0.3$  yielding a full detector acceptance relation of

$$\langle P_T \rangle \sim 0.3 \text{Im}\xi. \quad (3.23)$$

In order to see the connection between  $\text{Im}\xi$  and the effective parameters of New Physics appearing in the coefficients of generic exotic interactions, interesting results can be obtained with following effective four fermion Lagrangian:

$$\begin{aligned} L = & - \frac{G_F}{\sqrt{2}} \sin\theta_C \bar{s}\gamma_\alpha (1 - \gamma_5) u \bar{\nu}\gamma^\alpha (1 - \gamma_5) \mu \\ & + G_S \bar{s}u\bar{\nu} (1 + \gamma_5) \mu + G_P \bar{s}\gamma_5 u \bar{\nu} (1 + \gamma_5) \mu \\ & + G_V \bar{s}\gamma_\alpha u \bar{\nu}\gamma^\alpha (1 - \gamma_5) \mu + G_A \bar{s}\gamma_\alpha \gamma_5 u \bar{\nu}\gamma^\alpha (1 - \gamma_5) \mu + h.c.. \end{aligned} \quad (3.24)$$

Here,  $G_S$  and  $G_P$  are the scalar and pseudo-scalar coupling constants and  $G_V$  and  $G_A$  are the exotic vector and axial-vector coupling constants, respectively. Tensor interactions are neglected.  $\text{Im}\xi$  is caused only by the interference between the SM term and the scalar term, namely by the complex phase of  $G_S$  [20] [21], which can be written as

$$\text{Im}\xi = \frac{(m_K^2 - m_\pi^2) \text{Im}G_S^*}{\sqrt{2}(m_s - m_u) m_\mu G_F \sin\theta_C} \quad (3.25)$$

where  $m_s$  and  $m_u$  are the masses of the s-quark and u-quark, respectively. Thus,  $P_T$  can constrain the exotic scalar interactions.

### 3.3 Theoretical Predictions

#### 3.3.1 Standard Model

The very small SM contribution for  $P_T$  is one of the important motivations of this experiment. A T violating amplitude arises from the relative phases between diagrams or complex coupling constants in a diagram. Since only a single element of the CKM matrix,  $V_{us}$ , is involved for the W - exchange semi-leptonic  $K_{\mu 3}$  decay in the SM, no CP violation appears in first order. As discussed in Chapter 3.1 this is a general feature for vector and axial vector type interactions. The SM contribution comes only from higher order effects. The possible size of its contribution was suggested qualitatively in [22] to be less than  $P_T < 10^{-6}$ . An actual value based on the lowest-order vertex radiative corrections to the  $\bar{u}\gamma_\mu(1 - \gamma_5)sW^\mu$  vertex (Fig 3.3) has been presented in the textbook (Bigi and Sanda [23]). This has been estimated to be less than  $10^{-7}$ . This fact constitutes the main motivation for a  $P_T$  experiment as a search for New Physics. As shown in the next section, considering FSI effects, an observation of a non-zero  $P_T$  implies unambiguously the existence of CP violation mechanisms beyond the SM.

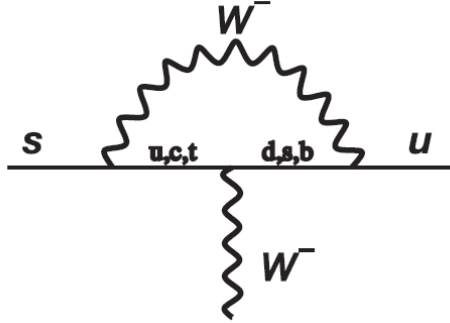


Figure 3.3: Radiative corrections in the  $K_{\mu 3}$  decay

#### 3.3.2 Final state interactions

Strictly speaking, the observation of measured non-zero  $P_T$  value does not mean T violation automatically. Spurious  $P_T^{FSI}$  can be induced by final-state-interactions (FSI). This has been a concern in  $P_T$  experiments for quite some time. In the case of  $K_{\mu 3}^0$  decays, the FSI are mainly due to electromagnetic interactions. The FSI contributions to  $P_T$  in the present case are much smaller than those in  $K_{\mu 3}^0$  decay, which has two charged particles interacting in the final state,  $P_T^{FSI}(K_{\mu 3}^0) \sim 10^{-3}$ , the FSI in  $K_{\mu 3}^+$  has been extensively investigated. The single-photon contribution to  $P_T^{FSI}$  in  $K_{\mu 3}^+$  decay is due to the imaginary part of the two-loop diagrams. An

example is shown in Fig 3.4. This was estimated more than 20 years ago to be  $P_T^{FSI} \leq 10^{-6}$  [1]. Quite recently two-photon exchange contributions to  $P_T^{em}$  have been studied in Ref. [2], where the transverse polarization is proportional to the imaginary parts of the diagrams shown in Fig 3.4. The value of  $P_T^{em}$  averaged over the Dalitz plot was found to be less than  $10^{-5}$ . Thus, a non-zero  $P_T$  in the range of  $10^{-3} \sim 10^{-4}$  will constitute a clear signal of contribution from a New Physics.

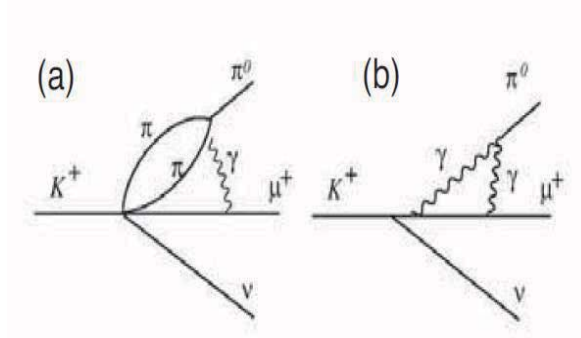


Figure 3.4: (a) One of the diagrams of the final state interactions contributing to  $P_T^{em}$  ; from one photon exchange calculated in Ref. [1] and also (b) one of the diagrams from two photon exchanges calculated in Ref. [2].

### 3.3.3 Multi-Higgs doublet model

Multi-Higgs doublet models have been considered as the minimum and natural extension of the SM with one Higgs doublet, and a number of papers [24], [25], [23] have applied this models to  $P_T$ . In the class of models without tree-level flavor changing neutral current, new CP violating phases are introduced in the charged Higgs mass matrix if the number of doublets is more than two. The couplings of the quarks and leptons to the Higgs boson is expressed in terms of the Lagrangian [24, 25]

$$L = (2\sqrt{2}G_F)^{\frac{1}{2}} \sum_{i=1}^2 \{ \alpha_i \bar{u}_L V M_D d_R H_i^+ + \beta_i \bar{u}_R M_U V_{dL} H_i^+ + \gamma_i \bar{\nu}_L M_E e_R H_i^+ \} + h.c., \quad (3.26)$$

where  $M_D$ ,  $M_U$ ,  $M_E$  are diagonal mass matrixes,  $V$  is the CKM matrix, and  $\alpha_i$ ,  $\beta_i$  and  $\gamma_i$  are the new complex coupling constants associated with the charged Higgs interactions. The coefficients,  $\alpha_i$ ,  $\beta_i$  and  $\gamma_i$  can have complex phases, and  $P_T$  is calculated as

$$Im\xi = \frac{m_K^2}{m_H^2} Im(\gamma_1 \alpha_1^*) \quad (3.27)$$

where  $\alpha_i$  and  $\gamma_i$  are the quark and lepton couplings to the lightest charged Higgs boson. The E246 result [10] yielded  $|Im(\gamma_1\alpha_1^*)| < 544(m_H/GeV)^2$  as the most stringent limit for this parameter. It is also constrained by the semileptonic decay of the  $B$  meson [26],  $B \rightarrow \tau\nu X$  but the result is less stringent than the  $P_T$  constraint. According to the recent result on  $B \rightarrow \tau\nu$  [27], its impact on this model is now being checked. Other constraints on this model come from the neutron EDM ( $d_n$ ),  $b \rightarrow s\gamma$  [26] and  $b \rightarrow sl\bar{l}$  [28] complementing the  $P_T$  result in a different manner, since these channels limit  $Im(\alpha_1\beta_1^*)$ . These two parameters are related as  $Im(\alpha_1\beta_1^*) = -(v_3/v_2)^2 Im(\gamma_1\alpha_1^*)$  through the ratio of the vacuum expectation values  $v_2$  and  $v_3$ . An interesting scenario assumed in [24] has  $v_3/v_2 \sim m_{tau}/m_t \sim 1/80$  thus making  $P_T$  the most sensitive test of the three Higgs doublet model. Another important feature of this model is the prediction of  $P_T$  in the radiative decay  $K^+ \rightarrow \mu^+\nu\gamma$  ( $K_{\mu\nu\gamma}$ ). The following expression was obtained [20],

$$P_T(K_{\mu\nu\gamma}) \cong -0.1 \frac{m_K^2}{m_H^2} Im(\gamma_1\alpha_1^*) \quad (3.28)$$

with the same sign as  $P_T(K_{\mu 3})$  but with different size. E246 provided a result [10], however it lacked good statistics. Although the final state interaction is large  $\approx 10^{-3}$ , also we may pursue this mode at J-PARC in the future.

### 3.3.4 SUSY models

A number of other models also allow  $P_T$  at an observable level without conflicting with other experimental constraints. Hence a non-observation of  $P_T$  can constrain these models. Some Minimal Super-symmetric Standard Models (MSSM) allow sizable values. One interesting case is the model discussed by G.-H.Wu and J.N.Ng [29]. In this model the complex coupling constant between the charged Higgs boson and strange and up-quarks is induced through squark and gluino loops. Then, the  $P_T$  value when the muon and neutrino momenta are at right angles, is given as

$$P_T^{H^+} \approx 3.5 \times 10^{-3} I_{H^+} \frac{p_\mu}{E_\mu} \frac{(\mu + A_t \cot \beta)}{m_g} \frac{(100 GeV)^2}{M_H^2} \frac{Im[V_{33}^{H^+} V_{32}^{D^*} V_{31}^{U^*}]}{\sin \theta_C} \quad (3.29)$$

for  $\tan\beta \approx 50$  (For the meanings of various symbols see Ref. [29] except to note that we assumed the top quark mass to be 180 GeV). If we allow large flavor mixing coupling in the squark-quark vertices, there is an allowed parameter region for large  $P_T$ . The E246  $P_T$  upper bound corresponds to  $M_H > 140 GeV$ . In view of the many assumptions made, this bound should be considered as a qualitative estimate [29]. It is noteworthy that  $P_T(K_{\mu 3})$  and  $P_T(K_{\mu\nu\gamma})$  have opposite signs in this model.

Another interesting SUSY model is the R-parity violating model [30], in which the interactions are described by the Lagrangian using the  $\lambda_{ijk}$ ,  $\lambda'_{ijk}$  and  $\lambda''_{ijk}$  coef-

ficients of the super potential as

$$\begin{aligned}
L &= \frac{1}{2} \lambda_{ijk} [\bar{\nu}_{L_i}^c e_{L_j} \tilde{e}_{R_k}^* + \bar{e}_{R_k} \nu_{L_i} \tilde{e}_{L_j} - (i \leftrightarrow j)] \\
&+ \lambda'_{ijk} [\bar{\nu}_{L_i}^c d_{L_i} \tilde{d}_{R_k}^* + \bar{d}_{R_k} \nu_{L_i} \tilde{d}_{R_j} + \bar{d}_{R_k} d_{L_j} \tilde{\nu}_{L_i} \\
&- \bar{e}_{R_i}^c u_{L_j} \tilde{d}_{R_k}^* - \bar{d}_{R_k} e_{L_i} \tilde{u}_{L_j} - \bar{d}_{R_k} u_{L_j} \tilde{e}_{L_i}]
\end{aligned} \tag{3.30}$$

by assuming  $\lambda''_{ijk}=0$  because of the non-observation of proton decays. Here the subscripts  $i(k)$  are the slepton family indices. There are two kinds of contributions to  $P_T$ ; one is from slepton exchange and the other is from down-type squark exchange. They are given, respectively as

$$\text{Im}\xi^l = \sum_i \frac{\text{Im}[\lambda_{2i2}(\lambda'_{i12})^*]}{4\sqrt{2}G_F \sin\theta_c(m_{\tilde{l}_i})^2} \cdot \frac{m_K^2}{m_\mu m_s} \tag{3.31}$$

$$\text{Im}\xi^d = \sum_i \frac{\text{Im}[\lambda'_{21k}(\lambda'_{22k})^*]}{4\sqrt{2}G_F \sin\theta_c(m_{\tilde{d}_i})^2} \cdot \frac{m_K^2}{m_\mu m_s} \tag{3.32}$$

Thus, the parameters of  $\text{Im}[\lambda_{2i2}(\lambda'_{i12})^*]/m^2$  and  $\text{Im}[\lambda_{21k}(\lambda'_{22k})^*]/m^2$  are constrained. These are many experimental constraint for  $\lambda_{ijk}$  and  $\lambda'_{ijk}$  [31], but for the relevant four combinations of  $\lambda(\lambda')^*$  and  $\lambda'(\lambda)^*$  the constraint from other experimental limits are not stringent enough, thus  $P_T$  determines their limits as a function of their mass scale  $m$ .

### 3.4 J-PARC TREK Experiment

The 40 year history of  $P_T$  experiments show a rather slow improvement in the upper limit. This is due to two reasons: the first point is that the statistical sensitivity of an asymmetry measurement scales as  $1/\sqrt{N}$ , while the single event sensitivity in rare decay experiments scales as  $1/N$ . The second reason is the nature of this high precision experiment which must be conducted and analyzed very carefully. The understanding and reduction of systematic errors can only be achieved step-by-step. We prefer to this approach to the J-PARC experiment and to proceed in the goal of SM+FSI signal region of  $10^{-5}$  in steps.

The E246 result was essentially statistics-limited. The largest systematic error in the error table, which was due to multiple scattering, is statistical in nature and it could have been improved as was foreseen at the start of the E246 experiment. We propose to improve the E246 result by at least a factor 20 ( $\delta P_T < 2 \times 10^{-4}$ ), by improving both the statistical and the systematics uncertainties. This sensitivity puts the experiment well into the region where new physics effects can be discovered, and even a null result would set tight constraint on various theoretical models. If warranted, further sensitivity improvement towards  $10^{-5}$  will be proposed in the

next stage after we have been convinced of the possibility to pursue this experiment to such a high precision region. In that sense, the TREK experiment may be considered as a prelude to precision frontier experiments at J-PARC.

We have to upgrade the E246 detectors.

- New polarimeter system (an active polarimeter + muon polarimeter magnet) is adopted to reduce the  $\mu^+$  multiple scattering and the uncertainty of the magnetic field in the polarimeter.
- New electronics and read-out, in particular CsI(Tl) read-out, systems will be adopted to handle the higher event rates.
- Additional tracking GEM chambers for charged particle is adopted for improving the uncertainty in the determination of decay planes
- A smaller target with finer segmentation is adopted in order to improve the uncertainty in the  $K^+$  stop position.

We plan to perform the TREK experiment using the K1.1BR beamline in the Hadron Experimental Hall in J-PARC. At present we are waiting for the realization of high power accelerator operation (currently  $\sim 5\text{kW}$  intensity beam for slow extraction is available), and after finishing another experiment (E36) at K1.1BR which can be performed with lower accelerator power, we will start to perform the TREK experiment. The preparation of all the detectors is in progress.

### 3.4.1 Experiment design

In order to overcome the limitations of the E246 experiment, several improvements to the detector system must be undertaken.

The TREK experiment will be performed using a toroidal spectrometer setup in conjunction with a stopped  $K^+$  beam at the low momentum separated kaon beamline K1.1BR in the Hadron Experimental Hall of the J-PARC 50GeV synchrotron. The spectrometer consists of an iron-core superconducting toroidal magnet with 12 gaps. The setup is shown in Fig 3.5. The  $K^+$  beam will be stopped in an active target located at the center of the magnet.  $K_{\mu 3}$  decays will be identified by detecting a  $\pi^0$  with a CsI(Tl) barrel surrounding the active target, a muon with a charged particle tracking system consisting of GEM chambers (C0, C1), MWPCs (C2, C3 and C4) and with particle identification by means of time-of-flight (TOF). This arrangement will enable a measurement of the decay pions ranging over all directions covering all regions of the decay phase space for a given  $\mu^+$  momentum. As described next, this scheme allows for a "double ratio" measurement and, thus, a number of systematic errors can be suppressed. The CsI(Tl) barrel has 12 holes to admit charged particles into the magnet gaps. Since the barrel does not cover the full  $4\pi$  solid angle, not all events will have the two photons from  $\pi^0$  decay detected.

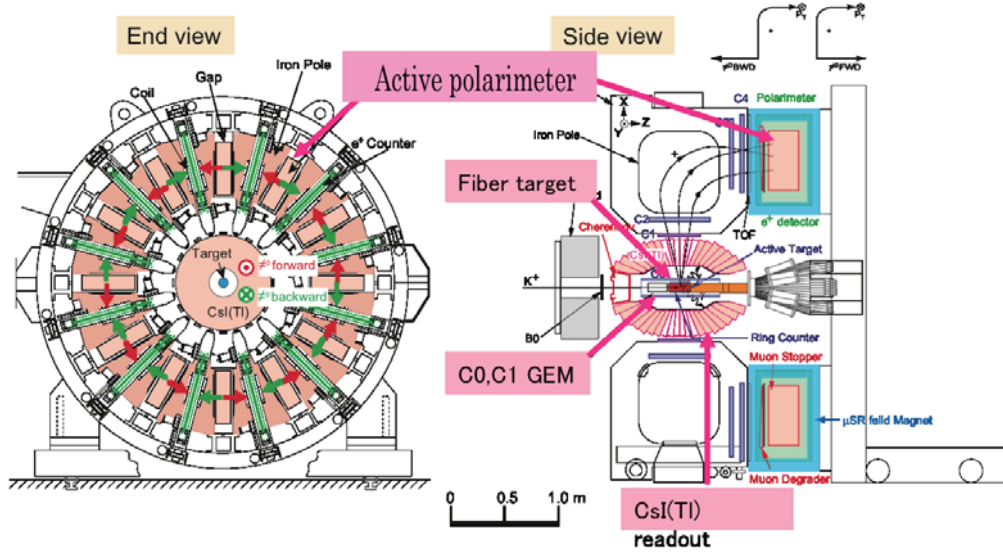


Figure 3.5: End and side views of the TREK detector system

However, one photon with relatively large energy can also be used to determine the  $\pi^0$  momentum. Muons are bent by about 90 deg, momentum-analyzed, and then they enter the muon polarimeter system. After passing through a spectrometer and Cu degrader, the muons are finally stopped in the active polarimeter. The muon polarization is measured by means of the decay positron asymmetry. When  $\pi^0$ s are detected in the forward (FWD) or the backward (BWD) directions relative to the beam axis, the transverse component  $P_T$  lies in the azimuthal directions in each polarimeter clockwise (*cw*) or counterclockwise (*ccw*), respectively. Thus, the magnitude of the transverse polarization  $P_T \sim \vec{\sigma}_\mu \cdot \vec{p}_{\pi^0} \times \vec{p}_{\mu^+}$  can be measured as the azimuthal asymmetry of positron emission, namely a *cw* and *ccw* emission rate difference.

Our aim is to perform an experiment which, in comparison to E246, will have about 10 times more acceptance (using active polarimeter described next chapter), about 20 times the integrated beam flux, and few times higher analyzing power to achieve nearly a factor at least 20 improvements in the statistical sensitivity, i.e.,  $\delta P_T$  (one  $\sigma$  limit)  $\sim 10^{-4}$ .



### 4.1.2 Passive polarimeter for E246

The advantage of the passive system was its simplicity with the consequence of very small systematic errors associated with the analysis. The systematic cancellation scheme when the asymmetry was summed over the 12 sectors was also based on the use of positron counters as clockwise and counterclockwise counters at the same time. However, this was done at the cost of positron detection acceptance and polarization analyzing power.

### 4.1.3 The analysis method of the E246 polarimeter

The transverse polarization was measured as an asymmetry defined as

$$A = \frac{N_{cw} - N_{ccw}}{N_{cw} + N_{ccw}} \quad (4.1)$$

with the clockwise (*cw*) and counterclockwise (*ccw*) counts,  $N_{cw}$  and  $N_{ccw}$ , respectively. A measurement to determine the null asymmetry  $A_0$ , was also needed to ensure an accurate  $P_T$ . For measuring the null asymmetry, the data, which did not require the  $\pi^0$  direction ( *fwd* direction or  *bwd* direction), could be used. In this case, the data could include  $K_{\pi 2}$  events. After confirming the data quality from the null asymmetry measurement, the transverse polarization ( $P_T$ ) measurement could be performed. In order to take better quality  $P_T$  data from  $K_{\mu 3}$  decay, a double ratio method was performed for two opposite kinematic situations which correspond to the  $\pi^0$  direction, respectively ( *fwd/bwd*). Paying attention to just one  $e^+$  counter, it could count both  $N_{cw}$  and  $N_{ccw}$ . This means that the efficiency of this counter is canceled out when we sum up the 12 sector data with 12-fold azimuthal symmetry. This method played an important role in reducing the systematic errors. However, several difficulties still remained. When the transverse asymmetry was measured, it was essential to consider the fact that the muon stopping distribution could affect the asymmetry very strongly. In particular, a shift along the  $y$  direction was critical. The asymmetry  $A_0(y)$  for the muons is shown in Fig 4.2.

The effect of the shift on the asymmetry is  $\delta A = k \times \delta \langle y \rangle$  with  $k = 0.015/\text{mm}$  for the average shift  $\delta \langle y \rangle$ . Considering such a spurious effect, the asymmetry was analyzed differentially using the  $y$ -information from the C4 chamber which was located in front of the polarimeter. The  $y$  direction of the T violating asymmetry  $A_T(y)$  was calculated as

$$A_T(y) = \frac{1}{2} \left( A^{fwd}(y) - A^{bwd}(y) \right), \quad (4.2)$$

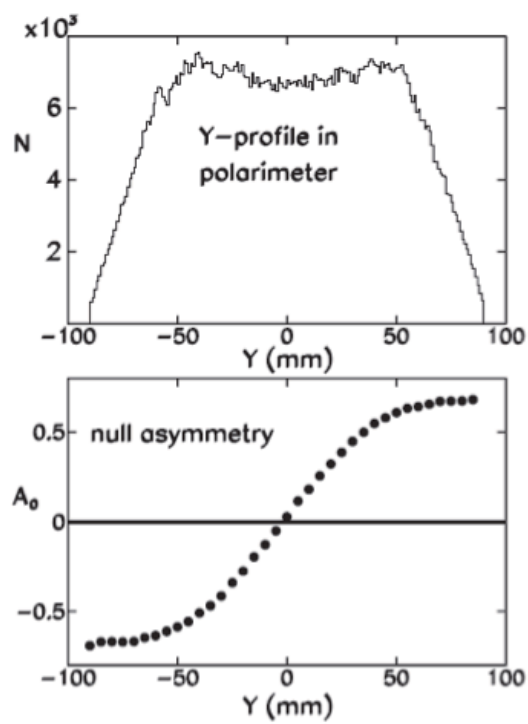


Figure 4.2: Incident muon  $y$  distribution in the stopper measured by the C4 chamber (top), and the intrinsic geometrical asymmetry for those muons (bottom).

with the  $y$ -dependent  $fwd$  and  $bwd$  asymmetries

$$\begin{aligned} A^{fwd}(y) &= \frac{1}{2} \left[ \frac{N_{cw}^{fwd}}{N_{ccw}^{fwd}} - 1 \right], \\ A^{bwd}(y) &= \frac{1}{2} \left[ \frac{N_{cw}^{bwd}}{N_{ccw}^{bwd}} - 1 \right]. \end{aligned} \quad (4.3)$$

Here,  $N_{cw}(y)$  and  $N_{ccw}(y)$  are the event number distributions from C4- $y$ . The T violating polarization at each  $y$  point was then extracted using the relevant analyzing power function of  $\alpha(y)$ , which was determined by the polarimeter structure, and detector acceptance, as

$$P_T(y) = \frac{A_T(y)}{\alpha(y) \langle \cos \theta_T \rangle}. \quad (4.4)$$

The attenuation factor,  $\langle \cos \theta_T \rangle$  determined by the average of the angles  $\cos \theta_{\pi^0}$  is independent of  $y$ . This scheme corresponds to the case in which a number of sliced muon stoppers were inserted and the polarization measurements were done for each stopper. The final  $P_T$  result for one data set was obtained as the statistical average of  $P_T(y)$  as

$$\begin{aligned} P_T &\equiv \langle P_T \rangle = \int P_T(y) w(y) dy, \\ &= -0.0017 \pm 0.0023(stat) \pm 0.0011(syst), \end{aligned} \quad (4.5)$$

with the normalized weight function of  $w(y) \sim 1/\sigma_{P_T}^2(y)$ . Thus,  $P_T$  was unaffected by the muon stopping distribution in the stopper.

As mentioned above, it was impossible to avoid the effect of multiple scattering and there is no way to know the decay vertex. This means that some systematical uncertainties are still remaining. Actually, the uncertainty from muon multiple scattering was larger than any other systematic error. Considering these points, the E246 polarimeter should be improved in order to achieve a sensitivity of  $\delta P_T \sim 10^{-4}$ .

#### 4.1.4 Requirements for the active polarimeter

In comparison with the situation of E246, where the positron signals were associated with non-negligible constant background events, the new active polarimeter determines the muon stopping position for each event, and this in turn, renders the experiment free from the systematic error associated with the ambiguities in the muon stopping distribution. Since the decay positron tracks are measured, the decay vertices will be determined event-by-event.

The active polarimeter should have the following functions and advantages.

- Determination of the muon vertices event-by-event

Detection of the decay positrons in all directions by a polarimeter with a large acceptance with nearly  $4\pi$  solid angle. In E246 the positron counter solid angle was limited to about 10% on each side. The detector acceptance becomes 10 times larger, even though the sensitivity does not scale by this factor. The ability to measure the positron emission provides the possibility to use not only the *fwd/bwd* pion scheme but also the *left/right* pion scheme which was not possible in E246.

- Measurement of the positron emission angle

The asymmetry changes as function of both the positron emission angle and the energy. A weighted analysis brings about a significant increase in the analyzing power resulting in higher sensitivity. It is of interest to note that this superior performance is achieved in the case of measuring the positron emission angle precisely.

The requirements for the polarimeter design are listed below.

- The polarimeter should have a large muon stopping efficiency in relatively small volume. This means that the polarimeter should be made of a material with high average density.
- On the contrary, the polarimeter should enable a clean detection of positrons without interections such as bremsstrahlung or annihilation in flight. This means that the polarimeter should be made of a material with low average density.
- A drift chamber is an adequate choice of the detector.
- The cell structure is essentially determined by the fine structure of the stopper. Thus, the stopper has to be designed taking this point into account.
- Optimization for the azimuthal field arrangement sets the highest priority to the *fwd/bwd* pion analysis. Thus, the stopper structure must be optimized for the *cw/ccw* asymmetry measurement.
- Internal cancellation mechanism against any local inefficiency is essential for the polarimeter. The *cw/ccw* inefficiency cancellation scheme of the E246 experiment is maintained by using the polarimeter.



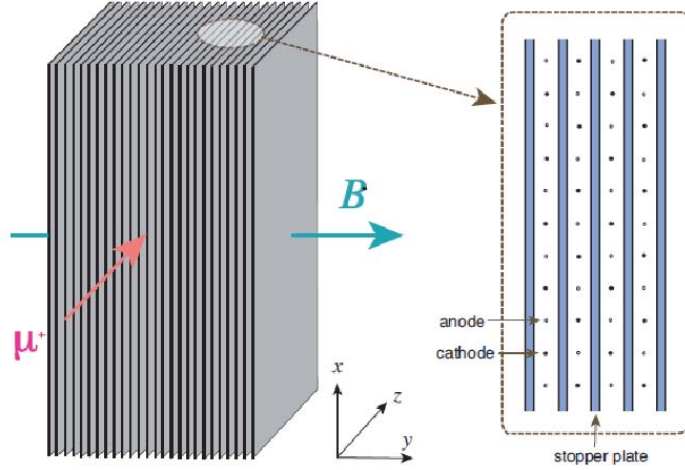


Figure 4.4: Muon stopper made of parallel plates which serve also as drift chamber cell structure

compromise the chamber performance. Regarding the tracking resolution a series of Monte Carlo simulation calculations have been performed.

One of the important things to consider was determining the selection of the stopper material. The analyzing power, defined as  $A_T/P_T$ , should be as large as possible to obtain the highest sensitivity in the experiment. The requirements were, without any initial polarization loss during stopping and without any significant spin relaxation. Considering the decay positron interaction, the material should also be a light element. Hence, the E246 experiment adopted a pure Al plate with 99.99% purity. However, in the TREK experiment, pure Al is not suitable since the muon stopper material itself constitutes a component of the active polarimeter drift chamber mechanical structure. In this case the stopper plates have to be rigid enough as a structural component, while pure Al is too soft and easily deformed. The most important prerequisite is good spin polarization behavior which could be investigated with a real muon spin relaxation measurement.

By studying Al and Mg material at TRIUMF in 2007, A5052 was selected as the frame material of the polarimeter and pure Al(JIS1100) was also selected as the stopper material.

After a charge division study, at the Fuji Test Beam Line (FTBL) at KEK in 2008, we adopted SUS304 for the sense wires. The details of this experiment is described in Ref. [32], and charge division method is mentioned in Appendix B. The result was that 2 mm in the position resolution  $\sigma$  is good enough for our

requirement, and the sense wire which has  $1.9\text{ K}\Omega$  intrinsic resistance can fulfill the requirements.

In the positron track reconstruction analysis, there were difficulty caused by a rectangle cell structure. In a case of the rectangle, the shape of the equi-drift time line is very complicated. Hence, it is difficult to determine the drift velocity precisely. As a result, the calculation of the drift velocity have to rely on the simulation if we pursue higher position resolution. Another possible issue is due to its geometry. Misalignment if the plates with respect to the average muon incident direction may result in a situation where muons enters in the plates dorminantly from one side, leading to an asymmetry of positron efficiency in the transverse direction. The beamtest studying for this plate model was performed in Autumn 2009, and the evaluation was summarised in Ref. [33].

### 4.3 Muon Tube Polarimeter - MTP -

The other choice of TREK polarimeter is tube type polarimeter, MTP. I describe the beamtest to evaluate the performance of this model in Chapter 5, and describe analysis in Chapter 6.

The MTP is composed of a stack of drift tubes. Like the plate type polarimeter the MTP can track not only incident particles but also the decaying particles. Hence the MTP can define exactly emission angle for each event, and so is free from the systematic error associated with the ambiguities in the muon stopping distribution that were present in E246.

Table 4.2 shows the detail of the MTP. The tube thickness was decided based on a Geant4 simulation, for stop muon middle of the MTP. The equi-drift time plane is completely circular, hence it is easier to reconstruct tracks compared to the rectangular cells. Broken wires do not affected to the other wires. Compared with the plate type, the MTP has fewer wires, so it's easy to read-out, data-taking, analysing, and manufacturing. I have summarized the comparison between two models in table 4.1.

Tracking methods are

- YZ-plane : equi-drift time plane (use of tracking)
- X-axis : charge division



Figure 4.5: MTP (size: 865mm  $\times$  284mm  $\times$  330mm, 75kg)

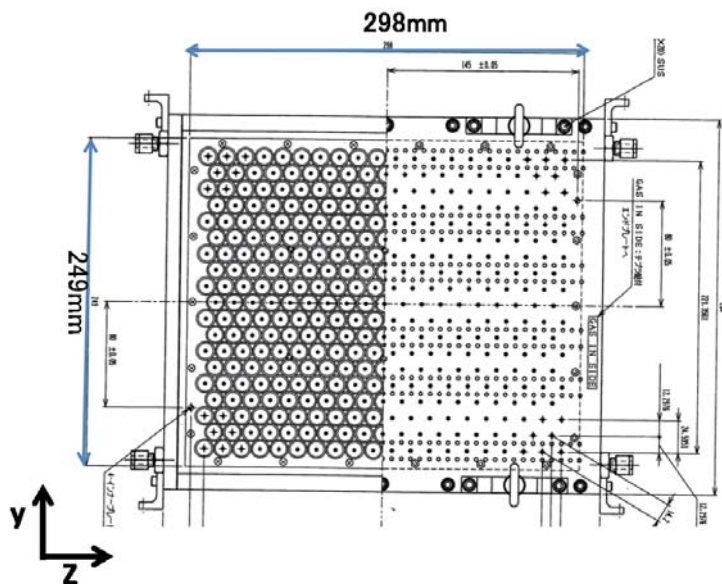


Figure 4.6: MTP YZ-plane

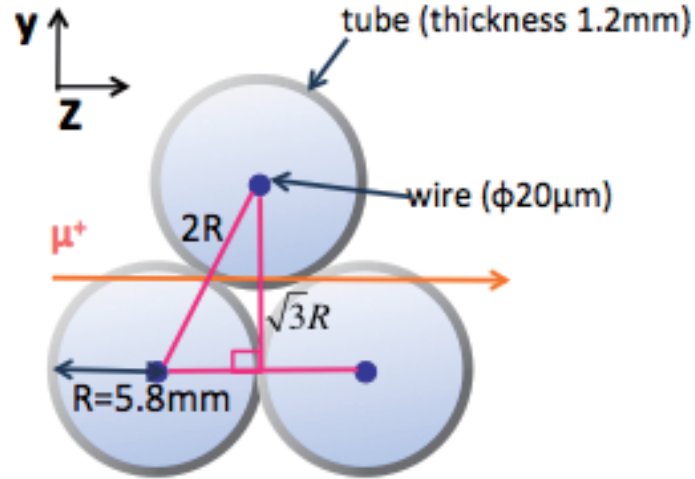


Figure 4.7: Schematic end view of the MTP

Table 4.1: Comparison between plate type and tube type

	Plate type	Tube type
number of sense wires	$\sim 500$ channel	371 channel
number of potential wires	$\sim 500$	none
distance between sense wires	16mm	14.2mm
equi-drift time line	complicated	circle
drift analysis for small angle	good	good
drift analysis for large angle	not good	good
tracking for small angle	good	good
tracking for large angle	not good	good
manufacturing	easy	not very easy
maintenaice	not good	good

Table 4.2: Detail of MTP spec

spec size	284mm $\times$ 865mm $\times$ 330mm
gas	Ar : Ethane = 50 : 50
sence wire	SUS304 20 $\mu\text{m}$
number of channels	371
read-out AMP	ASB card
material density / full volume	24%

### 4.3.1 Drift tube

A drift tube detects charged particles by means of gaseous ionization and its detection. Passing through gas, charged particles ionize the gas molecules, atoms and lose energy due to Coulomb interactions. The average differential energy loss (loss per unit length) is expressed by the Bethe-Bloch Formula in the framework of relativistic quantum mechanics, and can be written follows (in the electrostatic unit system):

$$-\frac{dE}{dX} = K \frac{Z}{A} \frac{\rho}{\beta^2} \left\{ \ln \frac{2mc^2 \beta^2 E_M}{I^2(1-\beta^2)} - 2\beta^2 \right\}, K = \frac{2\pi N z^2 e^4}{mc^2} \quad (4.6)$$

N : the Avogadro number

m, e : electron mass and charge

Z, A, and  $\rho$  : atomic number and mass, and the density of the medium

I : effective ionization potential

z : the charge

$\beta$  : the velocity in units of the speed of light c of the projectile

The rest energy of the electron is  $mc^2 = 0.511$  MeV, so  $K = 0.154$  MeV  $\cdot$   $cm^2/g$  for unit charge projectiles. The maximum energy transfer allowed in each interaction is  $E_M$ , and simple two-body relativistic kinematics gives the following.

$$E_M = \frac{2mc^2 \beta^2}{1 - \beta^2} \quad (4.7)$$

Gas detector produces the signal pulse arising from the energy loss of the incident particle in the gas after avalanche amplification. By these signal, the position of the trajectory and the energy deposit can be determined.

Two types of gas, base gas and quench gas are usually filled in a drift chamber. The former play a role as gas amplification to make the gain larger, and the latter does adjustment of amplification in order to defend electrical discharge, since it has large photon absorption cross-section. We used Argon for the base gas and Ethane for the quench gas mixture 50:50 for the the MTP operation.

There are 371 thin sense wire (SUS304,  $20\mu m$ ) stretched along the x axis of the MTP. When a strong electric field is applied around the electrodes it causes avalanche multiplication, boosting the signal amplitudes by several orders of magnitude. The electric field in one tube is at its maximum at the surface of the anode wire, i.e. sense wire, and rapidly decreases as  $r^{-1}$  towards the tube inner surface which play the role of the cathode. In order to produce high values of the field close to the anode, a thin wire is used.

In the region where the charges are produced by the primary interaction processes, a single primary electron proceeds towards the anode, on the contrary, the positive ion proceeds towards the cathode. The electric field near the wire is strong enough to start multiplication as the electrons come close to the anode. A drop-like avalanche develops surrounding the wire. Due to lateral diffusion and the small radius of the anode, the avalanche surrounds the wire as shown Fig4.8, electrons are collected and positive ions begin to drift towards cathode.

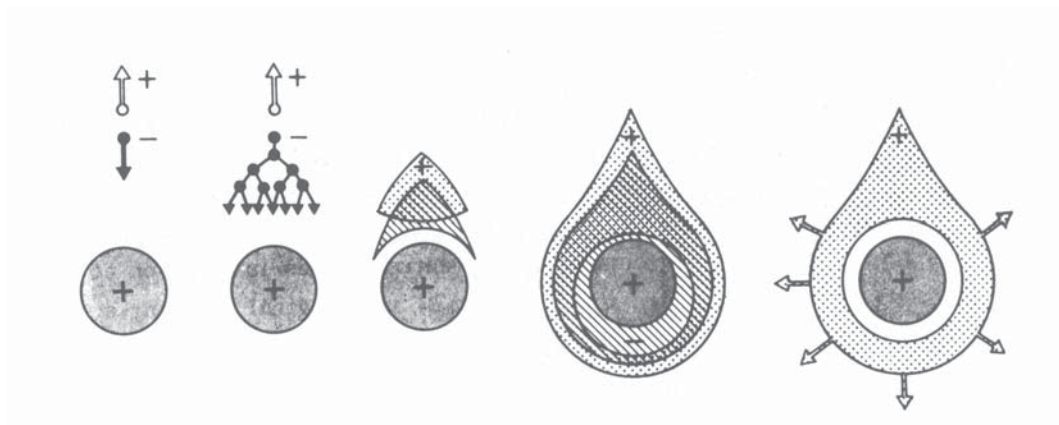


Figure 4.8: Time development of an avalanche in a proportional counter. [3]

#### 4.4 Muon polarimeter magnet

A uniform muon polarimeter magnet is essential for the TREK experiment, whereas a passive field was used by guiding and trimming the main field of the superconducting magnet in the E246 experiment. The unavoidable consequence was that there was a non-uniform strength distribution and a curved flux distribution at the stopper. A uniform field parallel to the  $P_T$  component provides the maximum analyzing power. Some requirements of the muon polarimeter magnet, size, field strength and uniformity, are as follows.

To accommodate the polarimeter with range stacks on both sides the parallel gap of the dipole magnet must be about 30 cm. The area is determined to produce a uniform field distribution in the polarimeter region. From the point view of

1. spin relaxation suppression,
2. stray field decoupling,

a strong field is preferable. However, the field is limited by the interference with the toroidal magnet, in particular with its SC coils. Point 2 is regarded as the

determining factor; assuming 0.3 Gauss of an unwanted component in the shielded magnet gap, a field strength of at least 300 Gauss is necessary to obtain a field alignment of  $10^{-3}$ . The field asymmetry across the median plane is important but a non-uniformity of  $10^{-2}$  in strength as well as in vector distribution is tolerable in the positron energy analysis.

A one sector prototype of the muon polarimeter magnet has been tested in the North Hall of KEK. After the symmetry measurement using the opposite coil-current method of the pole faces and coil without a return yoke, the magnet is now equipped with the low-weight yokes and a return yoke as shown in Fig4.9, and a normal field distribution with a uniformity good enough for the polarimeter has been achieved in the fiducial volume. This magnet can be applied to the TREK

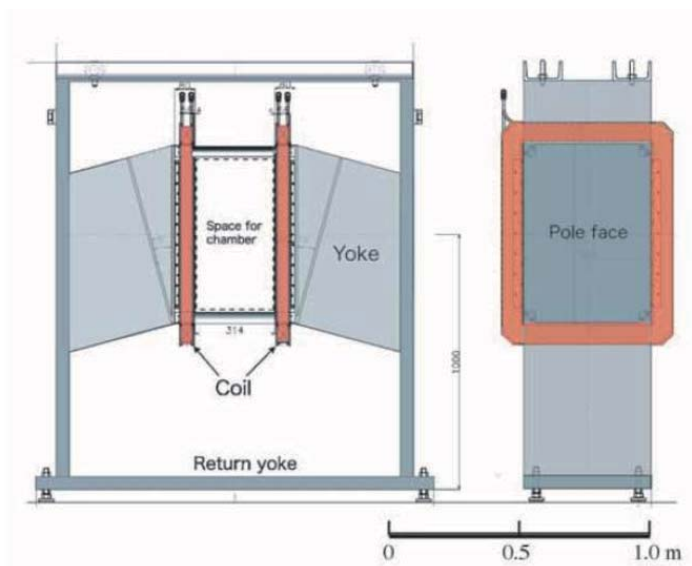


Figure 4.9: Schematic front view of the muon field magnet

experiment. It would be, however, necessary to compare the distribution with the 3D TOSCA calculation with the final realistic geometry. An improved shim system which realizes a larger field-flat volume might be possible. We don't know if the perpendicular  $B_x$  in the fiducial volume is small enough to suppress the systematic error due to  $\delta_z$  rotation, although its detailed estimate depends on the actual muon stopping distribution in the polarimeter and this is not yet known.

## 4.5 Systematic errors

In the TREK experiment, two sources of systematic errors will dominate. While one source is the misalignment of the detector elements, in particular of the muon

polarimeter, the other source will be given by the background contamination of muons from the decay-in-flight of  $K_{\pi 2}^+$  pions ( $K_{\pi 2}^+ - dif$  events).

- The effects of polarimeter misalignments, in particular the field rotation  $\delta_z$ , are not more relevant to the  $P_T$  determination. If necessary, they can be calibrated using data. Monte Carlo simulation studies assuming considerably large misalignments for the rotation parameters  $\epsilon_r, \epsilon_z, \delta_r$ , and  $\delta_z$  showed the associated systematic error to be smaller than  $10^{-4}$  in the discrepancy between the fit value and the input value.
- The influence of decay phase space distortion parameterized by the decay plane angular parameters  $\theta_r$  and  $\theta_z$  should be corrected. The error associated with these corrections is essentially a statistical one and is estimated to be far less than  $10^{-4}$  for both  $\theta_r$  and  $\theta_z$ . The validity of the correction method can be checked by introducing an artificial asymmetry in, for example, the kaon stopping distribution in the target to produce significant  $\theta_r$  and  $\theta_z$ .
- The error due to  $K_{\pi 2}^+ - dif$  background contamination can be suppressed by means of the new upgraded tracking system (Appendix C) down to less than  $5 \times 10^{-5}$ .
- There is a new potential source of error which was not present in E246, namely the error coming from the active polarimeter analysis. The effects of  $E_{e^+}$  and  $\theta_{e^+}$  ambiguities have to be suppressed to the level smaller than  $10^{-4}$ .
- The largest systematic error in E246, which was the ambiguity of muon stopping point due to scattering, does not exist in the TREK polarimeter anymore.

Other potential sources such as the misalignments of the tracking elements are regarded as rather harmless since correction based on the alignment calibration can be done accurately enough.

## Chapter 5

# Beam Test at TRIUMF

In order to investigate the detailed performance of the Muon Tube Polarimeter, we conducted a beam test experiment at TRIUMF, one of the world's leading sub-atomic physics laboratories, in Vancouver in Oct-Nov 2011. The main purpose was to see whether the MTP was suited for TREK experiment. The test program include basic evaluation of the drift tube, performance of muon and positron tracking, and performance as a muon polarimeter.

### 5.1 TRIUMF M11 beam line

TRIUMF has a 500 MeV cyclotron which produces the primary proton beams. Fig.5.1 shows the layout of the M11 beam channel. The primary proton beam strikes the meson production target T1, which is typically 1 cm thick graphite. The momentum of the channel is determined largely by the magnetic field of the two bending magnets B1 and B2. Focusing is achieved by using the 6 quadrupole magnets Q1 to Q6. There are also sextupole magnets available for a better focus, but these are not currently being used, since the object, and hence the image, is ill-defined in the absence of the septum magnet. The two quadrupoles Q1 and Q2 provide a double-focus at the midplane (focused in both horizontal and vertical planes), such that particles of the same momentum emanating beam the object point at various angles, will all intersect at the same point at this focus.

The midplane of the channel is a plane of momentum focus, such that particles of different momenta will come to a focus at different horizontal locations along this focal plane. The momentum dispersion is  $18 \text{ mm}/\% \Delta p/p$ .

With the horizontal slits open 90 mm full aperture, the beam channel admits a give value momentum bite. Also located at the midplane are a set of vertical slits which are considered to be fully open at 30 mm aperture when the septum was in operation, but which may need a larger opening to increase the flux. The total length of the M11 channel is 15.299 m, from the production target to the

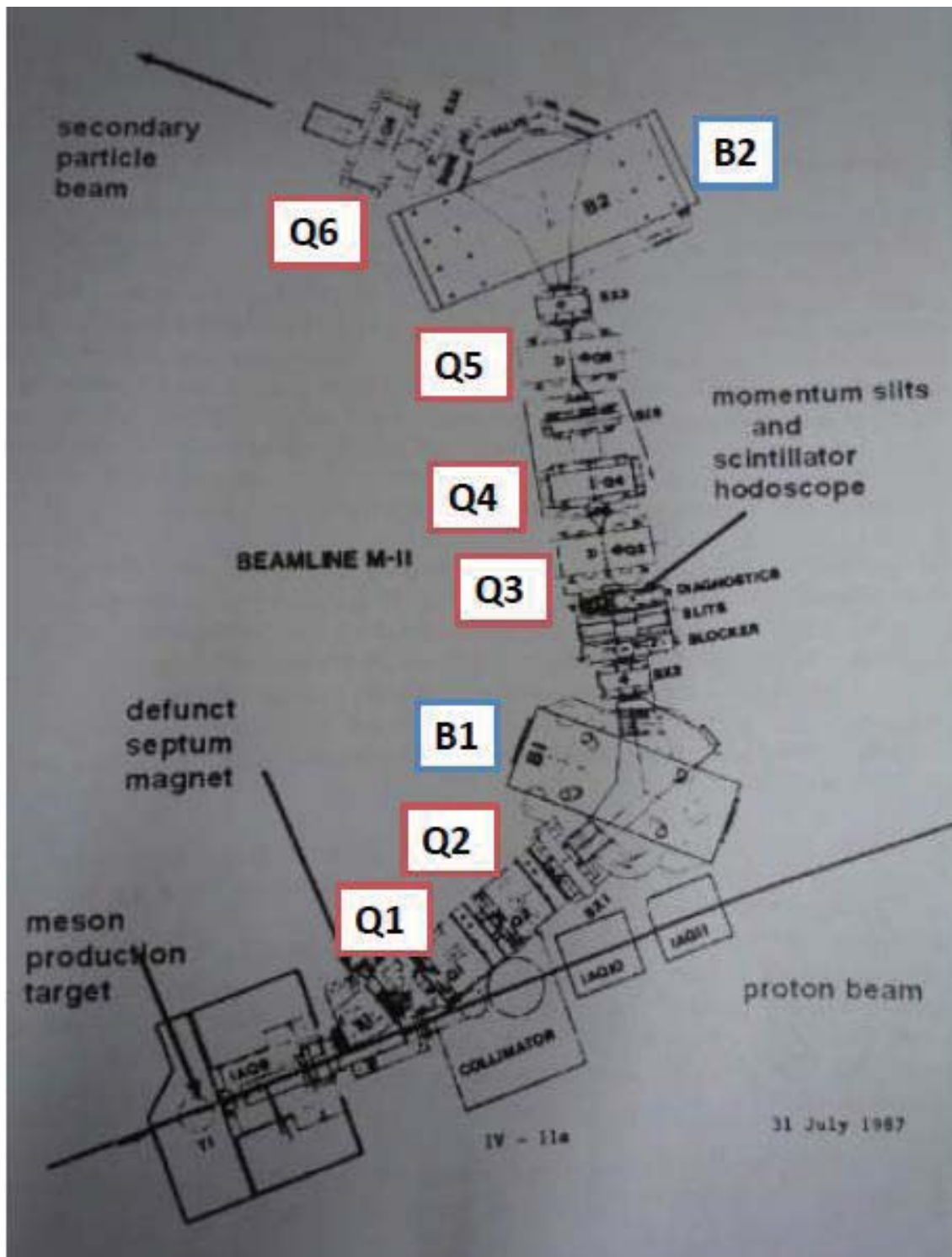


Figure 5.1: Layout of M11 beam channel

nominal final focus. The momentum range is from 60 MeV/c to 450 MeV/c.

Pions and muons travel down the M11 channel where they could be momentum selected. Particles with a momentum of 170 MeV/c were used for our beamtest.

## 5.2 Preparation

### 5.2.1 Preparation

We used an Ar/Ethane 50/50 flammable gas mixture for the MTP operation. The gas ratio is mainly associated with the drift velocity of the avalanche ions, so keeping a constant gas ratio was important. Before shipping from KEK to TRIUMF, we purged the MTP with pure Argon gas, which is not flammable, into the polarimeter. Prior to the installation of the MTP in the M11 experimental area, we pumped out the pure Argon gas and filled the MTP with the Ar/Ethane mixture gas.

After filling the gas, piping delivered the gas mixture from outside the area, and we could measure the gas inflow and outflow rates in order to monitor any gas leakage.

For a stable operation of MTP, it is important to set the proper high voltage. According to the HV curve (Fig 5.2), I used +1980 mV for the MTP, and the signal threshold was set at -30 mV by an analog signal check. The electric current of MTP was stable during the beam test, at  $\cong 1.8 \mu\text{A}$ .

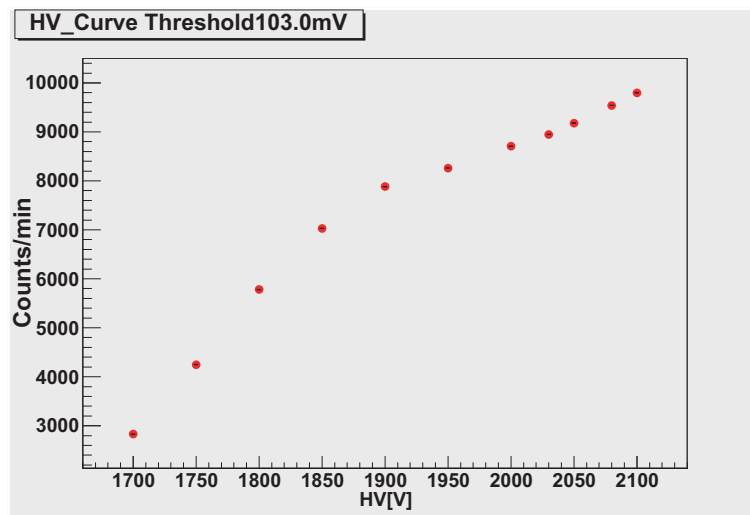


Figure 5.2: HV curve

### 5.2.2 Beam tuning

Fig 5.3 shows the experimental set up. We tuned the beamline to extract and

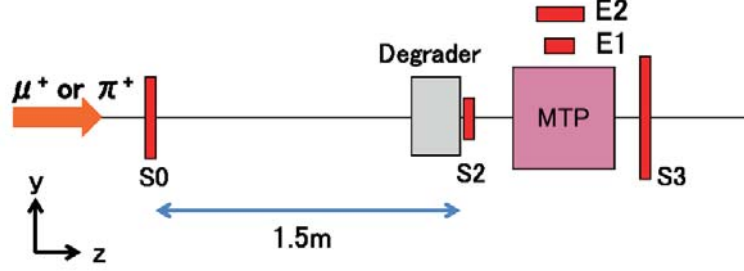


Figure 5.3: Setup for beam tuning and degrader tuning

separate both muons and pions with a fixed magnet current. We achieved particle identification by Time-of-flight (TOF) relative to the CP timing (Capacitive-Prove, proton bunch signal). This is a method of mass spectrometry by time measurement using the mass-to-charge. In beamline, particles have the same momentum as any other particle.

When the particle beta factor,  $\beta = v/c$ , where  $v$  is a particle's speed, it can be presented using particle's momentum  $p$ , its energy  $E$ , and rest mass  $m$  as follows:

$$\beta = \frac{pc}{E} = \frac{pc}{\sqrt{p^2c^2 + m^2c^4}} \quad (5.1)$$

Therefore, the time  $t$  spent when traveling a distance  $d$  is

$$t = \frac{d}{\beta c} = \frac{d\sqrt{p^2c^2 + m^2c^4}}{pc^2} \quad (5.2)$$

The distance of the M11 beamline is roughly 13 m.

Using TOF measurement, we tuned the beamline using S0, S2 and the CP timing. Here, M11 beamline produced proton bunches separated 43.37 ns. The CP on the 1A proton beamline sends out a pulse to each of the experimental areas whenever a proton bunch passes. We used this pulse for timing the arrival of the particles for TOF. The stop timing of TOF was determined by the CP signal. We found out that the beam momentum was best at 170 MeV/c, the pion contamination was larger at 180 MeV/c. We selected the particle timings for the pion gate 8 ns delay, for the muon gate 24 ns delay and for the fastest three mixed gate (muon, pion and positron) 38 ns delay. Table 5.1 shows the comparison of delay times.

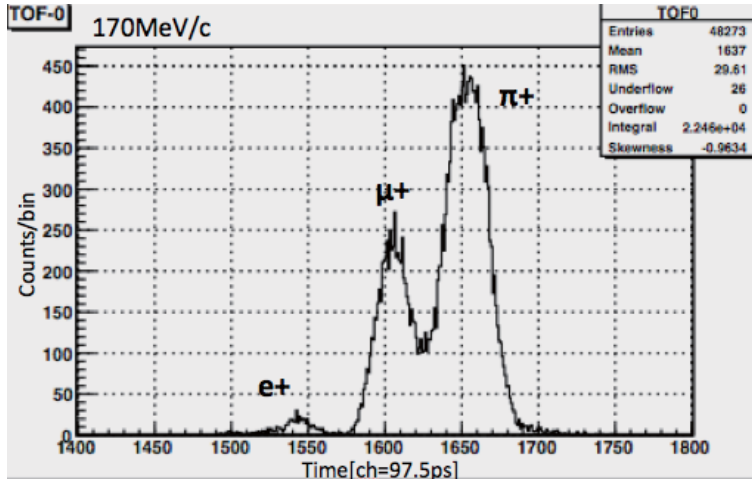


Figure 5.4: TOF spectrum at 170 MeV/c

### 5.2.3 Experimental setup

Fig 5.3, Fig 5.5 and Fig 5.6, Fig 5.7 show the configuration of the beam test. The data acquisition system consisted of 16 ASB cards, 16 VME-discriminator boards, 8 CAEN QDC modules and 4 CAEN TDC modules. These amplifiers and modules are explained in detail in Appendix D.

The trigger system consisted of several trigger counters. The trigger signal was selected by a triple coincidence which consisted of S0, S2 and the delayed TOF signals ( $S0 \times S2 \times \text{delayed TOF}$ ). The trigger timing was determined by the S2 counter, which was placed just before the MTP. The delay module located before the triple coincidence unit ( $S0 \times S2 \times \text{delayed TOF}$ ) could select the kind of particle according to the length of the delay cable. The TDC common stop was the same timing as the end of the trigger gate.

We scanned the MTP with the beam to see there were no broken wires, all of the 256 reading channels worked well. It was important to pay attention to check if there was wrong cabling or channel connection.

For TDC calibration, I checked the gap between the CP signals. Here, the frequency for the TRIUMF cyclotron was 23.06 MHz so the time separation of the beam pulses was 43.37 ns. The gap was 445 channels, so I got 1 channel = 97.46 ps (Fig 5.8).

Next, we made the beam particles stop in the middle of the MTP by adjusting

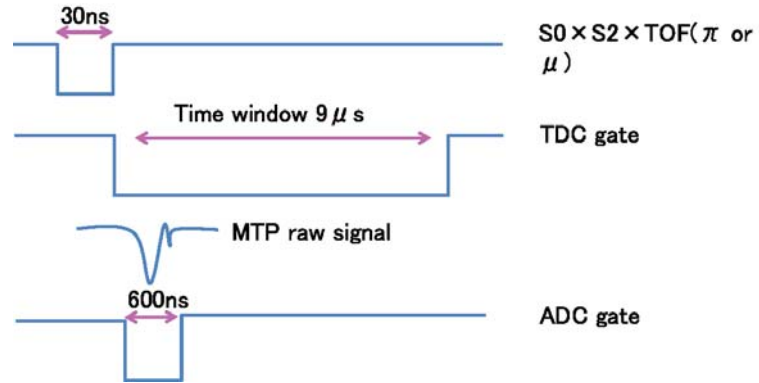


Figure 5.5: Timing chart

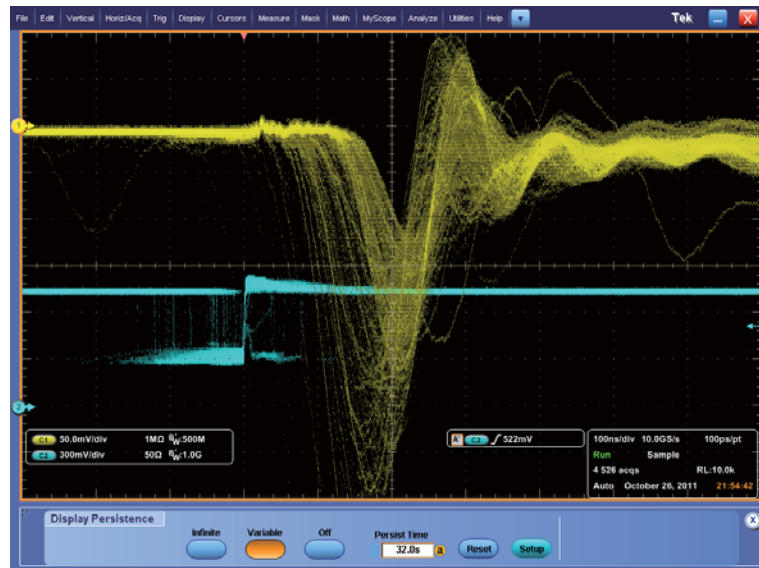


Figure 5.6: Typical chamber signal

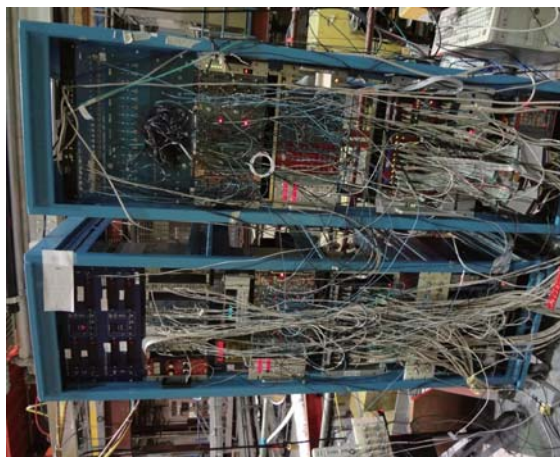


Figure 5.7: Configuration of the DAQ system

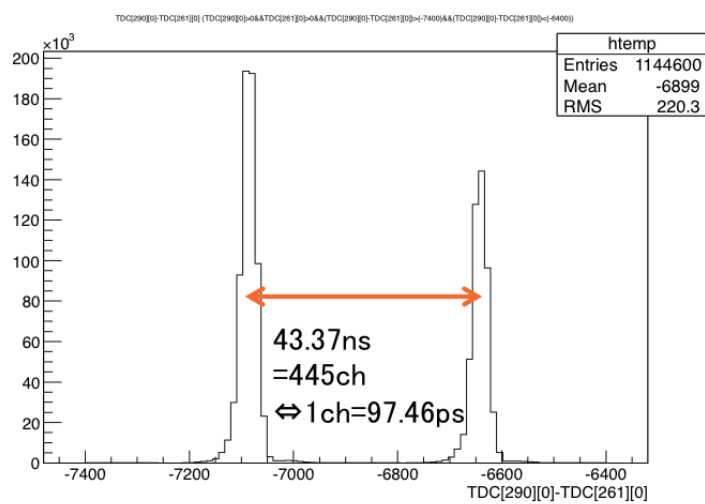


Figure 5.8: Gap between CP signals

the thickness of the Al degrader plates.

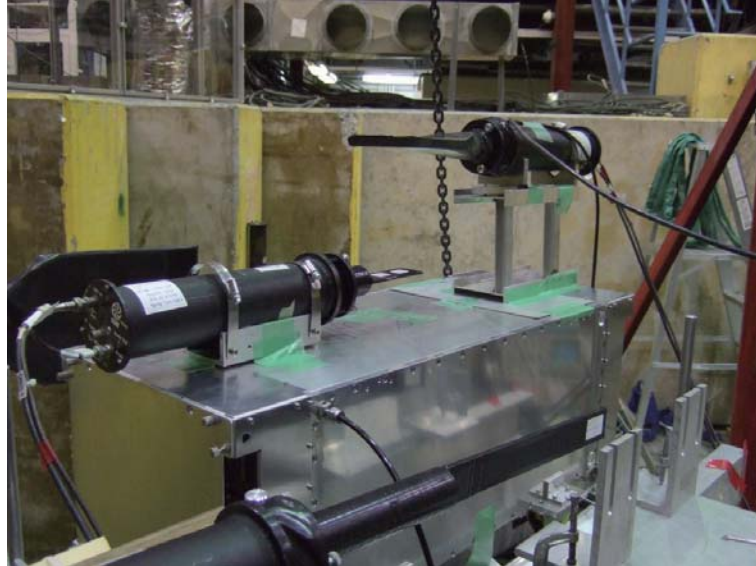


Figure 5.9: Degrader tuning ; Telescope (E1 and E2 counters) was placed on MTP

- beam tuning: to focusing beam on the trigger counter  
The S3 counter was used as a veto counter since we required the muon beam to stop in the middle of the MTP for our experiment. Here, we arranged E1 and E2 counters as a telescope pointing to the center of the MTP. The telescope was used in the range curve measurement.
- degrader tuning: to control the muon or the pion beam stopping position  
In the beam test, the entire volume of the MTP should be tested to determine whether or not the MTP detection efficiency depended on position. Hence, we varied the stopping position of the incident particles. In order to control the stopping position, some 0.5 and 1.0 inch size Al plates were used as the degrader. The Al degrader was located in front of the S2 counter.

In this measurement, a telescope (the set of E1 and E2 counters) was used and although it was just counting decay positrons, the number of counts correlated with the decay position. The telescope should be placed in the transverse direction relative to the other counters, so we placed it on top of the MTP. The number of telescope counts ( $E1 \times E2 \times TOF$ ) was normalized using the number of S0 and S2 coincidence ( $S0 \times S1$ ) counts.

When muon or pion stopped in the middle of the MTP, positrons should be emitted, so the thickness which enable the maximum telescope count rate is suitable. The results were the following;

For  $\pi^+$  : 1.5 inch Al (Fig 5.10)  
 For  $\mu^+$  : 3.25 inch Al (Fig 5.11)

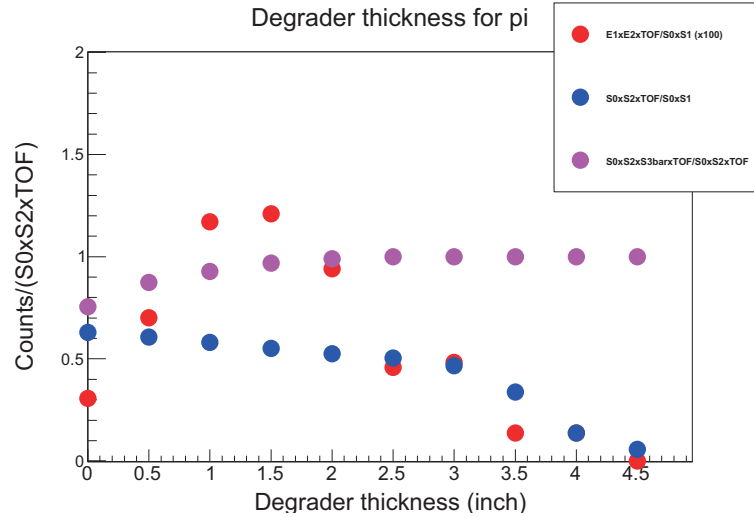


Figure 5.10: Results of the degrader tuning for  $\pi$

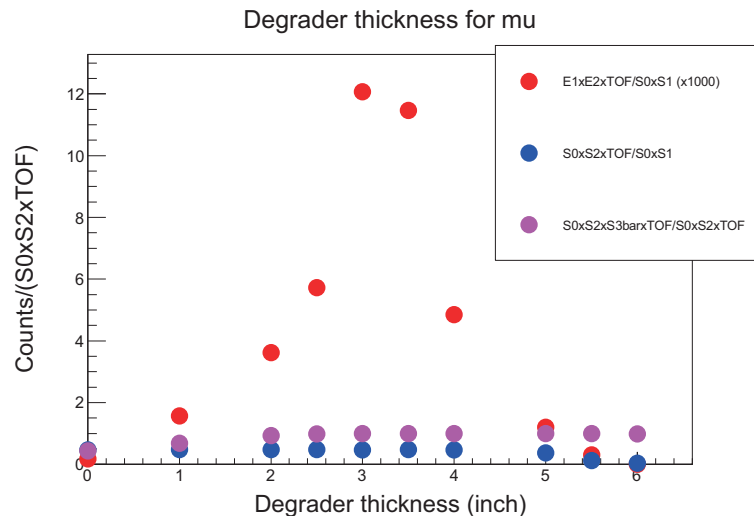


Figure 5.11: Results of the degrader tuning for  $\mu$

We found that the telescope timing presents that the decay positrons comes from the incident muons as expected(Fig 5.12).

Fig 5.13 shows the incident muon stopping point in the MTP. The last hit of

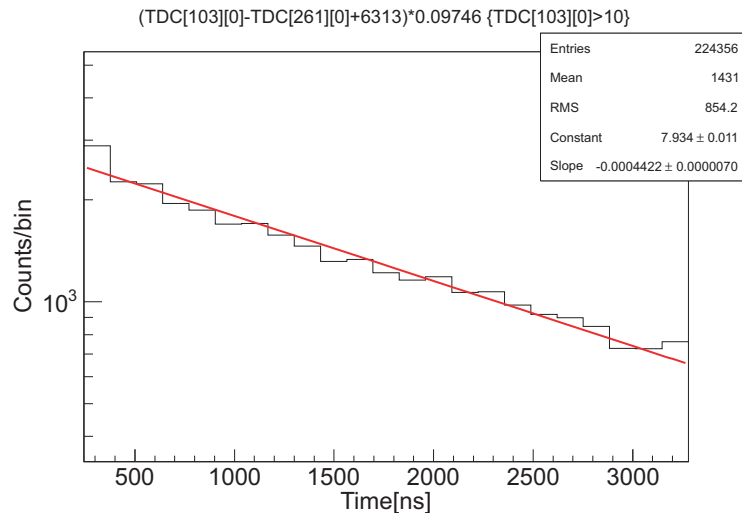


Figure 5.12: Muon decay curve: The parameter  $(1/\tau)$  corresponds to  $2.2\mu\text{s}$

the muons position are plotted in this Figure. We can see that the beam particles stopped at the center of the MTP.

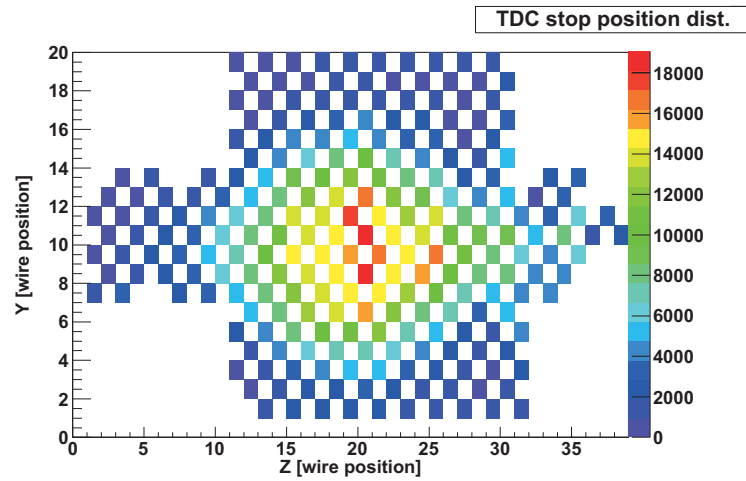


Figure 5.13: The confirmation of muon stopping area in MTP. The colored points means wire positions and all of the 256 channels worked well.

During beamtest, difficult things were below:

- The cabling was confusing as already mentioned.

- The connection between the cables and the modules were not very good, so we had to check the signal size by amps. This should be improved.
- The MTP signal was noisy without an Al foil shield. The cover of the mounting face for the cables and amps should more protected if there were no shield.

### 5.3 Measurements

We collected the data of different kinds as listed below.

- Normal run (using the muon trigger, high statistics  $\mu^+ \rightarrow e^+$  data collection)
- MTP rotated run (rotated forward and backward)
- Charge division run

Fig 5.14 shows the schematic view of charge division study set up and Fig 5.15 is the fiber scintillator to define the incident position of the muons with good precision. Reading both ends of wires, and moving x-direction.

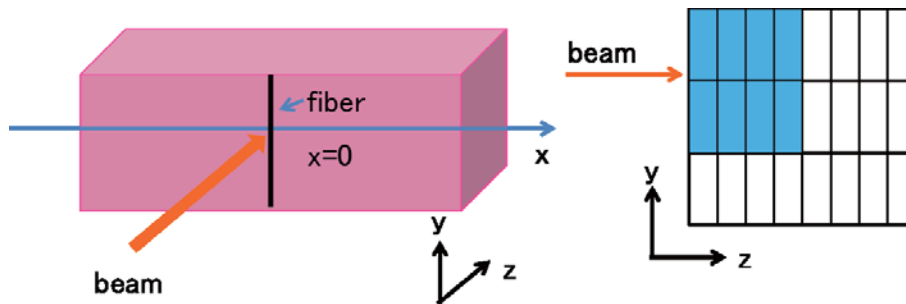


Figure 5.14: Schematic view of charge division study set up

- Pion run  
Degreder was set for the pion, and the pion trigger was used.
- $\mu$ SR run  
For the determination of the beam polarization. I describe in the next section.

### 5.4 $\mu$ SR measurement

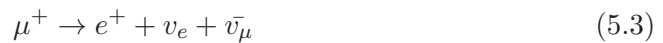
In order to determine the muon beam polarization of M11, we measured  $\mu$ SR, on the same place after MTP beam test. Since the muons with the momentum of 170 MeV/c generated upstream of the M11 beamline was considered to be the cloud muons. The polarization of cloud muons was not very well known.



Figure 5.15: Fiber scintillator for charge division study to define the incident position with a good precision

The muon is a spin  $-1/2$  particle, its mass is  $106 \text{ MeV}/c^2$ , and its lifetime is  $2.2 \mu\text{sec}$ . Its magnetic moment interacts with magnetic field. We use  $\mu\text{SR}$  measurement, Muon-Spin-Rotation or Muon-Spin-Relaxation, to know the polarization of the muon beam.

The muon's magnetic moment  $\vec{\mu}_\mu$  interacts with the local magnetic field  $\vec{B}_{loc}$  inside a solid. When a muon enters a material and stops there by ionization energy loss, the muon spin precess about the local magnetic field. When the muon decay via weak interaction, it emits a positron:



High energy positrons tend to be emitted in the direction of the muon spin. In order to detect the muon spin polarization  $P(t)$ , we can place counters which detect positron, typically, in the back and the front of the sample, and the asymmetry of their number of counts will tell us the direction of the spin. The number of hits at different times is plotted for each detector. When muons always feel same direction and same intensity of the magnetic field, the ensemble of the positron timing shows a cosine curve. Superimposed on the exponential decay of the muon is an oscillation showing extra counts as the muon's spin sweeps past the detector. If the field is non-uniform, the frequency of the muon spin is varies and the polarization to be gradually relaxed.

Fig 5.16. shows our set up for  $\mu\text{SR}$  measurement. We placed a magnet with 366 gauss instead of the MTP, and the Al sample (Fig 5.17), which was made of same material as the MTP, was placed at the center of the magnet. Using the same

experimental electronic circuit for the MTP beamtest, we changed the counters and their positions around the magnet. We used four counters, named S2, S3, E1 and E2, and I used the S3 counter for this analysis since its precession pattern was the most clear. S3 counter was located at the down stream of the Al sample along the beam direction.

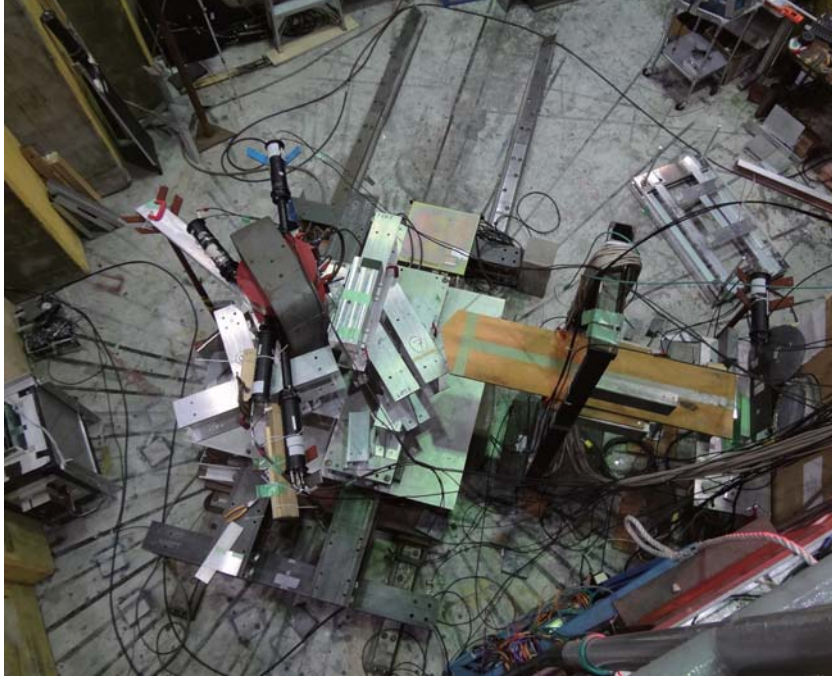


Figure 5.16: Set up for  $\mu$ SR measurement

Fig 5.18 shows the  $\mu$ SR precession pattern. The fitting function is following.

$$f(t) = N_0 \exp\left(-\frac{t}{\tau_\mu}\right) (1 + A \cos(\omega t + \phi)) + B.G. \quad (5.4)$$

$$\equiv p_0 \exp\left(-\frac{t}{p_1}\right) (1 + p_2 \cos(p_3 t + p_4)) + p_5 \quad (5.5)$$

Here,  $N_0$  is the normalization coefficient,  $t$  is the time,  $\tau_\mu$  is the muon lifetime,  $A$  is the amplitude corresponding to the asymmetry we want to determine, and  $\omega$  is the angular velocity,  $\phi$  is the initial phase, B.G. is the background.

According to the fitting result, asymmetry was  $5.694 \pm 0.005$  [%].

Considering time start origin, the initial spin direction could be known by the  $\mu$ SR spectrum and fitting result. The counters counted positrons, which were emitted by the muon and had the same direction of the muon spin by helicity conservation, so substitute the time when muons incident from fitting result Eq 5.5, we could determine the initial phase.



Figure 5.17: Al sample (5 cm  $\times$  2.4 cm  $\times$  2 cm )

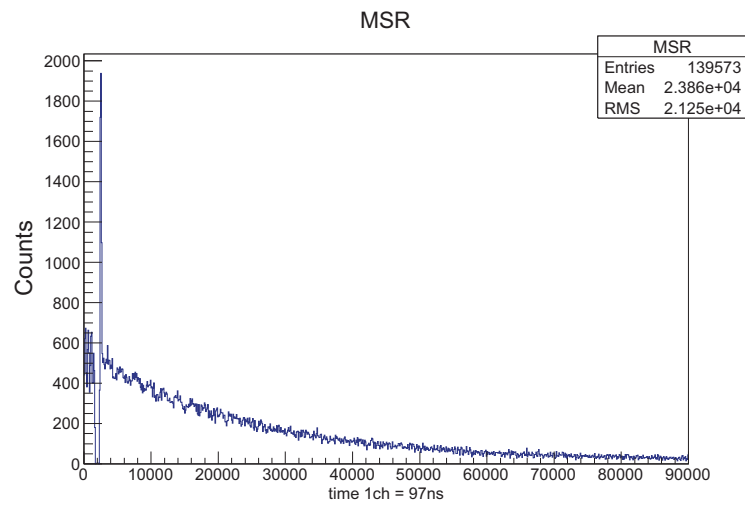
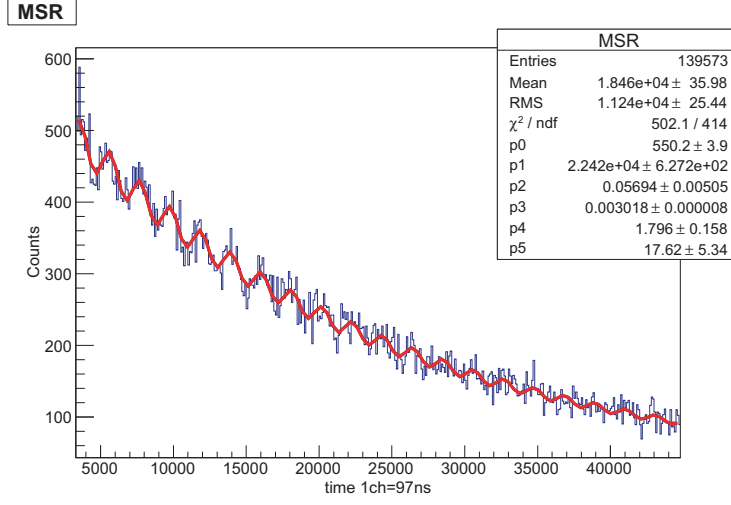


Figure 5.18: S3 counter timing spectrum : Muon stopping timing (the spike at  $\sim$  2500) and the oscillation pattern are seen.

Figure 5.19: Fitting result of the  $\mu$ SR oscillation spectrum

Using the TDC value of muon stopping time  $T_0 = 2548.3$ , calibrating muon stopping time for time zero, the relation between time  $t$  ns and  $T$  is

$$T = T_0 + \beta t, \quad \beta = 1/0.09746. \quad (5.6)$$

Therefore  $f(t)$  is expressed as

$$\begin{aligned} f(t) &= p_0 \exp\left(-\frac{T_0}{p_1}\right) \exp\left(-\frac{\beta}{p_1}t\right) (1 + p_2 \cos(p_3\beta t + p_3T_0 + p_4)) + p_5 \\ &= a_0 \exp\left(-\frac{t}{a_1}\right) (1 + a_2 \cos(a_3t + a_4) + a_5) \end{aligned} \quad (5.7)$$

where  $a_0 = p_0 \exp(-T_0/p_1) = 490.9 \pm 3.8$ .  $a_1 = p_1/\beta = 2185.1 \pm 61.1$  (ns) is muon decay constant, which is consistent with the PDG value (2.19698( $\mu$ s)).  $a_2 = p_2 = 0.05694 \pm 0.00505$  is the oscillation amplitude (5.69%).  $a_5 = p_5$ . Fig 5.20 shows the time calibrated fit function (Eq 5.7).

$a_3 = p_0\beta = 0.03097 \pm 0.00008$  is the muon spin angular frequency  $\omega = 2\pi f$ . Therefore the frequency was  $f = 4.929 \pm 0.013$ (MHz), which is consistent with the expected value 4.96 MHz, since the muon gyromagnetic ratio is 153.3 MHz/T and the magnetic field was 0.0366 T.

Those above-mentioned parameters were obtained from the measurement and fitting, now I wanted to know  $a_4$ , which is initial muon spin phase  $\phi_0$ .  $a_4 = T_0 p_3 + p_4 = 3.204 + 2\pi \pm 0.1783$ , and 3.204 rad = 183 degree. S3 counter was placed on the beam direction. Hence, it could be concluded that the muon spin was polarized backward, and forward muons.

In conclusion, the beam polarization we used was about 17% (= amplitude 5.69  $\times$  3) (Chapter 6.4.1) and backward polarized.

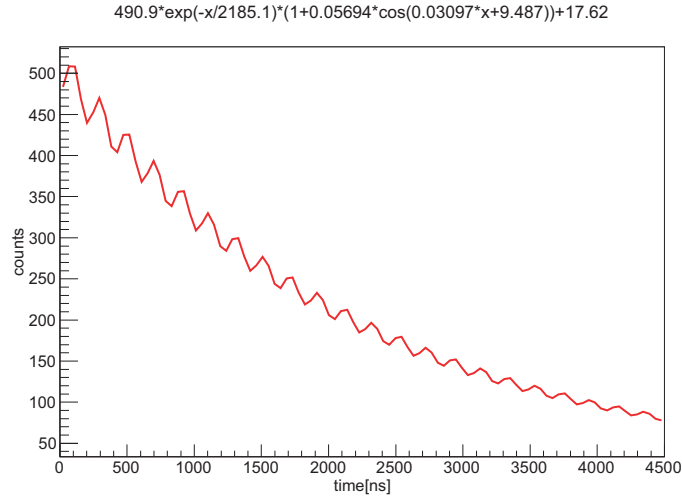


Figure 5.20: Calibrated time spectrum of the S3 signals.

Table 5.1: Comparison between particles

	$\pi^+$	$\mu^+$	$e^+$
Lifetime	26.033(5) ns	2.19703(4) $\mu$ s	$> 4.3 \times 10^{23}$ y
Mass (MeV/ $c^2$ )	139.56995(35)	105.8389(34)	0.51099907(15)
Charge (e)	+1	+1	+1
Spin ( $\hbar$ )	0	$\frac{1}{2}$	$\frac{1}{2}$
Delay (ns)	8	24	38

# Chapter 6

## Data Analysis

### 6.1 Basic Analysis

#### 6.1.1 Data quality

In order to evaluate the performance of the data, the time spectrum of the S2 counter was checked first. The S2 counter was used for determining the TDC stop timing. As shown in Fig 6.1, the time resolution of the S2 counter was obtained as  $\sigma = 1.276$  ns. This resolution was good enough to evaluate MTP signals because the typical sense wire time resolution scale, which was determined by the drift velocity of the avalanche ions and the cell structure, was much larger than the S2 counter time resolution scale.

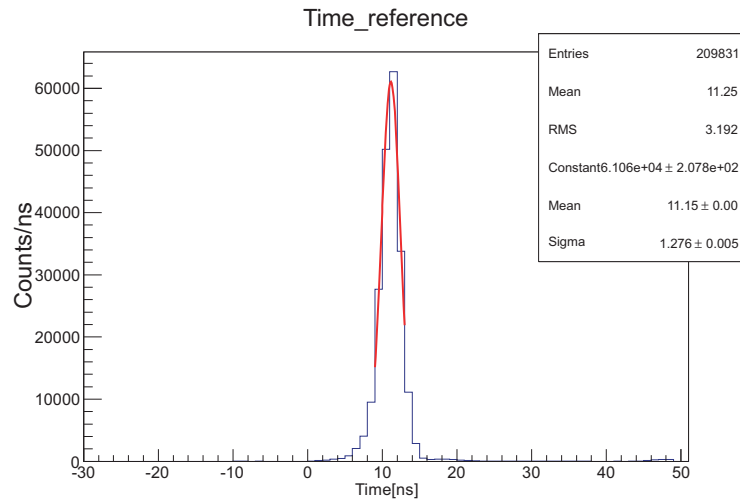


Figure 6.1: The S2 counter time spectrum. The S2 counter was used for determining the TDC stop timing.

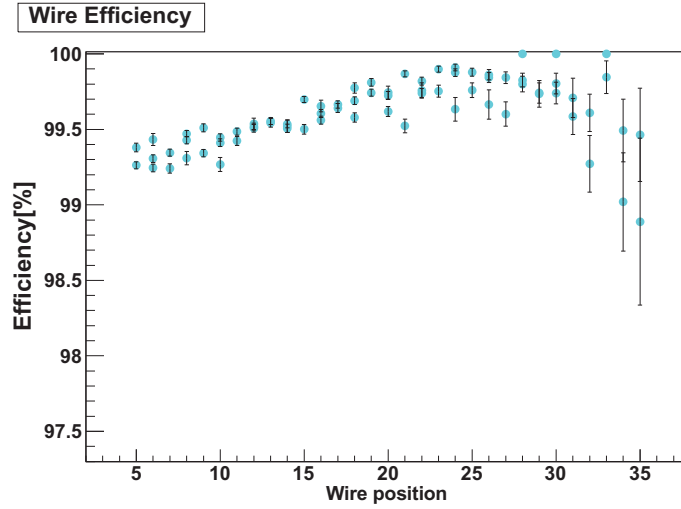


Figure 6.2: Wire efficiency

### 6.1.2 Wire efficiency

- Wire efficiency

It is important to have high detection efficiency as a tracker, which is usually required to have more than 99%. The tube efficiency was studied in the following way.

- The three wires parallel to the incident beam were selected for the whole volume of MTP.
- I examined whether the center of wire was tagged or not when both the surrounding wire were hit.

The wire efficiency of the chamber was evaluated using the muon beam data in our measurement, and is defined as follows and shown in Fig 6.2. Here the efficiency is shown as a function of  $z$  coordinate of the tube.

The decrease of the wire efficiency was due to the material density since this polarimeter plays a role as not only the detector but also the stopper. This polarimeter was made of material in order to stop the incident particles in the volume, this is a point of difference from other trackers. In general, a tracker should be made of light material in order to prevent secondary emission or particle scattering. Larger density like the MTP causes some bad tracks with large multiple scattering because it was difficult to prevent these effects. The apparent position dependence of the wire efficiency could be seen in Fig 6.2.

- Dependence of efficiency on drift distance

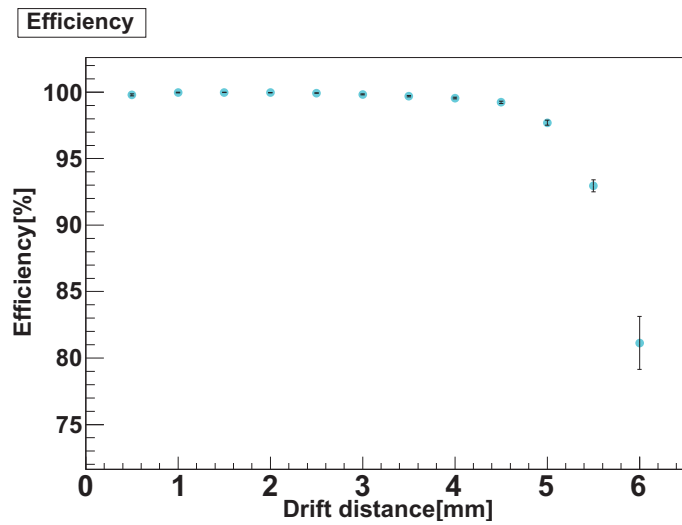


Figure 6.3: Efficiency as a function of the drift distance

The number of primary ionization, therefore the amount of collected charge on the wire, is proportional to the track length inside the tube, which varies as a function of the distance of the track from the wire.

I checked the uniformity of efficiency by means of computing the X-T relation, which I will explain in the next chapter, per unit mm. The definition of the efficiency here is:

- The three wires parallel to the incident beam were selected for the whole volume of the chamber.
- I checked each  $X_2(X_1, X_3)$  whether the center wire was hit or not (Fig 6.4).

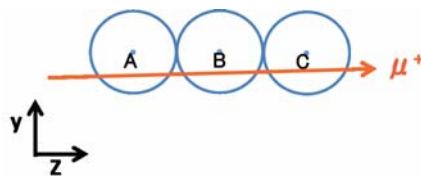


Figure 6.4: Schematic view of the wire efficiency of z-direction; the wire efficiency is expressed as (the middle of the A wire hit)/(all of the A, B, C wires are hit)

Fig 6.3 shows the result of the radial dependence of efficiency. It was good enough to detect ions from the whole volume of tube, since tube radius was 5.6 mm.

## 6.2 Drift time

In order to tracking precisely, it is important to define the time starting origin and to know the drift velocity of the electrons to draw drift circle and fit a track. The drift time distribution shows the expected shape for tube type drift chamber (Fig 6.5).

It was made by choosing  $1300 \text{ ch} = 124.15 \text{ ns}$  as the time origin which was the muon beam timing for a wire.

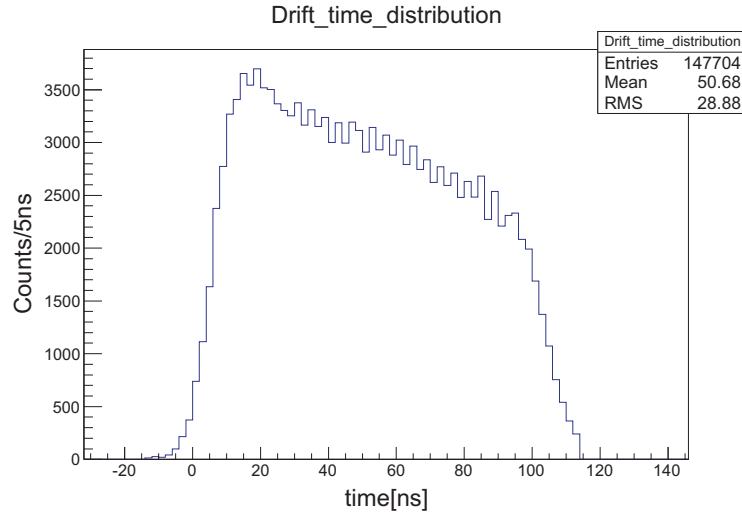


Figure 6.5: Drift time distribution

Assuming that the muons irradiated the tube uniformly, the drift distance is also uniform. I determined the following three parameters by means of fitting the drift time distribution.

- the time starting origin
- the relation between drift distance and drift time (X-T)
- the drift velocity

The slope of the drift time distribution is expressed as a linear function, with the rise time and fall time expressed as Fermi-Dirac function. The fitting function is:

$$f(\tau) = p_0 + \frac{p_1 ((\tau - p_3) + p_2)}{\left(1 + \exp\left(-\frac{\tau - p_3}{p_4}\right)\right) \left(1 + \exp\left(\frac{(\tau - p_3) - p_5}{p_6}\right)\right)} \quad (6.1)$$

- $p_0$  : background  
 $p_1$  : slope of the drift time distribution  
 $p_2$  : intercept  
 $p_3$  : time stating point  
 $p_4$  : width of the rising time  
 $p_5$  : max of the drift distance  
 $p_6$  : width of the fall time

Fig 6.6 shows the fitting result.

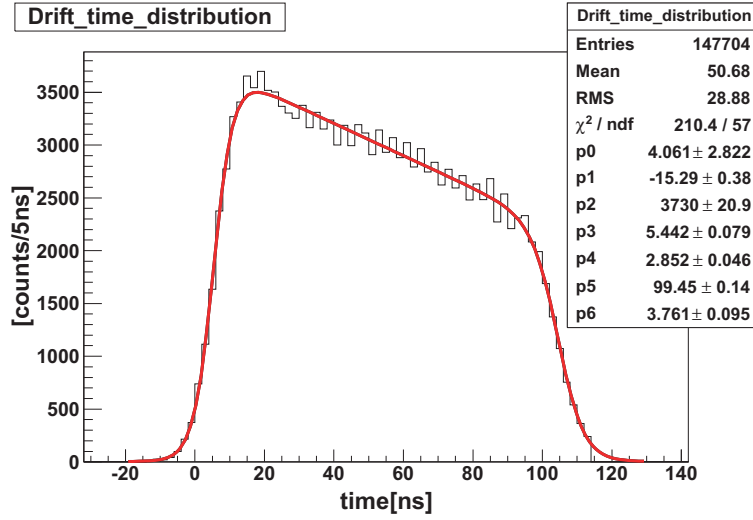


Figure 6.6: Fit to the drift time distribution

I obtained the X-T relation by an integration of the linear part of the distribution. The boundary condition was the position of the wire and tube surface as determined by the parameters  $p_3$  and  $p_5$ .

$$x(t) = (-1.50 \times 10^{-4})t^2 + (7.33 \times 10^{-2})t, \quad t \equiv \tau - p_3 \quad (6.2)$$

By differentiating this equation, the drift velocity could be determined.

$$\begin{aligned}
 v(t) &= \frac{d}{dt}x(t) \\
 &= (-3.00 \times 10^{-4})t + (7.33 \times 10^{-2})
 \end{aligned} \quad (6.3)$$

The average drift velocity was:

$$(\text{tube radius } 5.8 \text{ mm}) / (\text{maximum drift time } 110 \text{ ns}) = 50 \text{ } \mu\text{m/ns.}$$

Actually the velocity was not constant, you can see from drift time distribution, since there was gradient of the electric field from wire, but the average drift velocity was equal to the standard of a typical drift chamber filled with same mixed gases.

The assumed uniformity of the incident beam positions was confirmed by the drift distance distribution, which was made using the X-T relation. In addition, the drift distance distribution is consistent with the tube diameter, the approximation of the drift velocity was adequate.

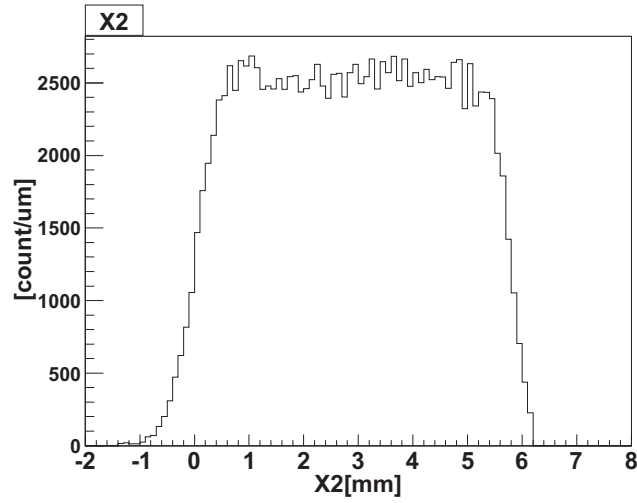


Figure 6.7: X2 distribution

Furthermore, to confirm this result, I checked by another X-T relation method. For adjacent three wires, I define a wire hit timings as  $t_1$ ,  $t_2$  and  $t_3$  and their drift distance as  $X_1$ ,  $X_2$  and  $X_3$ , respectively as shown in Fig 6.8.

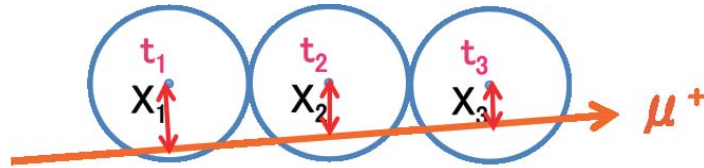


Figure 6.8: Schematic view of the definition of position for analyzing the X-T relation

Here, I derived  $X_2$  by two ways:

- Using equation 6.2 derived by fitting drift time distribution,  $X_2(t_2)$  is obtained directly from  $t_0$ .

- Alternatively  $X_2$  can be obtained from  $X_1(t_1)$  and  $X_3(t_3)$  using Eq. 6.4, assuming all the hits belong to a common straight track.

$$X_2 = (X_1 + X_3) / 2 \quad (6.4)$$

By comparing the relation between  $X_2(X_1, X_3)$  and  $X_2(t_2)$ , the consistency of the fitting result is confirmed.

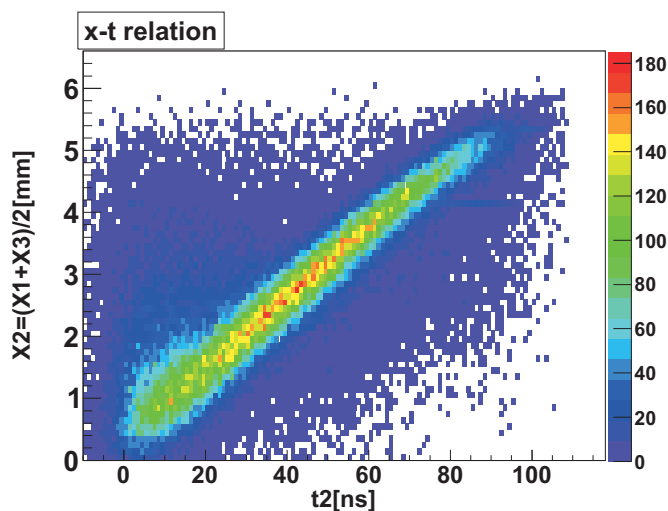


Figure 6.9:  $X_2(X_1, X_3)$  versus  $t_2$

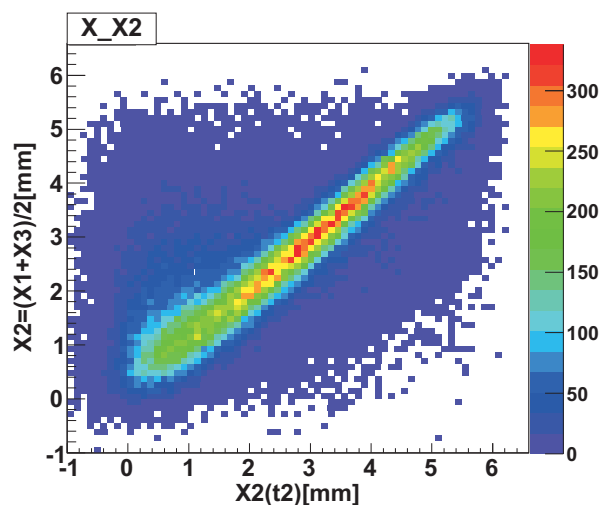


Figure 6.10:  $X_2(X_1, X_3)$  versus  $X_2(t_2)$

## 6.3 Tracking

### 6.3.1 Event selection

It was necessary to extract clean tracks with no-bias before the main analysis. The track reconstruction analysis and the asymmetry analysis require fine tracks extracted after some selections.

First of all, I classified the TDC hit timing in order to remove bad events. The incident particles, whose TDC is 0-2500 channels (1 channel = 97.5 ps), were categorized as "BEAM", and there no positron contamination due to the 500 ns delayed trigger gate. After "BEAM", the rest of the TDC data were categorized into 10 categories as 2500-10000 channels, ...,80000-90000 channels, and 90000-channels. There were some bad events which should be discarded, for example having some different timings which belong to more than 3 categories, respectively. I selected a true track which belong to both "BEAM" and the one of the other groups.

Next, I classified by geometry in order to eliminate some noise hits and to rescue inefficient hits. The incident track should be formed as a straight line, noise events which did not form a line were discarded. Since the decay positron has a low momentum, the positron tended to generate secondary particles, thus, a positron could make two lines. In this case, it was difficult to extract the true positron track, hence these events were also discarded.

I defined the last hit of the muon line as a vertex. Those events which have over two vertices should also be discarded since they could include some hits caused by secondary particles or event pile up.

### 6.3.2 Tracking algorithm

Using the X-T relation, drift circle of the point of hit wire( $y, z$ ) can be drawn. The line touching the drift circles can be estimated by the method of least squares. For this, following parameters were defined:

$$O_k = \frac{|ay + bz + c|}{a^2 + b^2} \quad (6.5)$$

$$E_k = Q_0(t - t_0)^2 + Q_1(t - t_0) \quad (6.6)$$

$$\sigma = \frac{p_0}{\sqrt{t - t_0}} + p_1 \quad (6.7)$$

where  $k$  is the identifications number of the wire.  $O_k$  is the distance between the sense wire and the fitting line.  $E_k$  is the radius of the equi-drift-time line, and  $\sigma_k$  is the fluctuation of the equi-drift-time line.

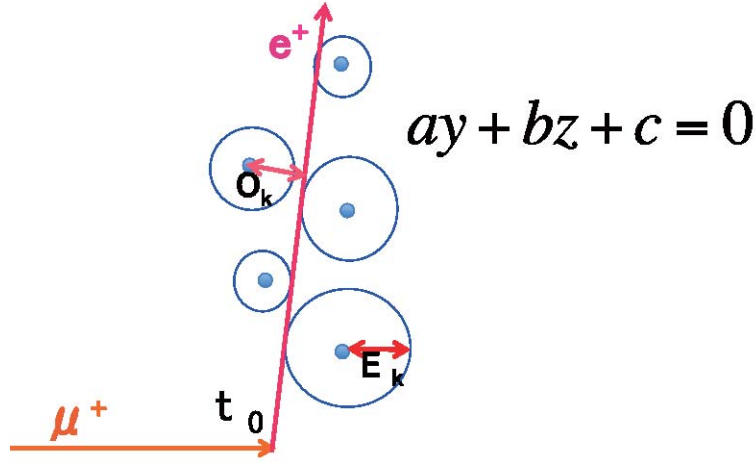


Figure 6.11: Schematic view of the track reconstruction

Here,  $E_k$  and  $\sigma_k$  have already been determined by the X-T relation.  $\sigma_k$  included a fluctuation of the incident angle, so the equi-drift-time line could be regarded as a full circle. Also, in order to consider multiple scattering, I used the positron in number order  $N_k = 1, 2, 3, \dots$  for a weight of chi-square. Therefore, chi-square was defined using these parameters as

$$\chi^2 = \sum_k \frac{(O_k - E_k)^2}{N_k \sigma^2} \quad (6.8)$$

Multiple scattering increases in proportion to the square root of the radiation length of the matter, the weight represents these things. The fitting of the decay positron was performed based on a principle of minimum  $\chi^2$ , using the ROOT TMinuit class. The MINUIT package acts on a multiparameter function to which one must give the generic name FCN, and offers the user a choice of several minimization algorithms. The MIGRAD algorithm is in general the best minimizer for nearly all functions. There was no information for determining the positron time origin  $t_0$  because we could not use a counter for measuring it. The positrons decay in the middle region of the MTP and  $t_0$  is different for each event. There were four free parameters corresponding to  $a$ ,  $b$ ,  $c$ , and  $t_0$ , more than 5 hits in a cell unit were required for the analysis. Thus, the fiducial volume of the polarimeter including the vertex cell was chosen as a small region.

The effects of using fitting weights or not are shown in Fig.6.12 and Fig.6.13. Without weights, the fitting line was pulled by the end of the hitting wire and this was not preferable because it means tracking was affected by multiple scattering. For the asymmetry analysis, we want to know the positron emitted angle uninfluenced by multiple scattering, so this method works well.

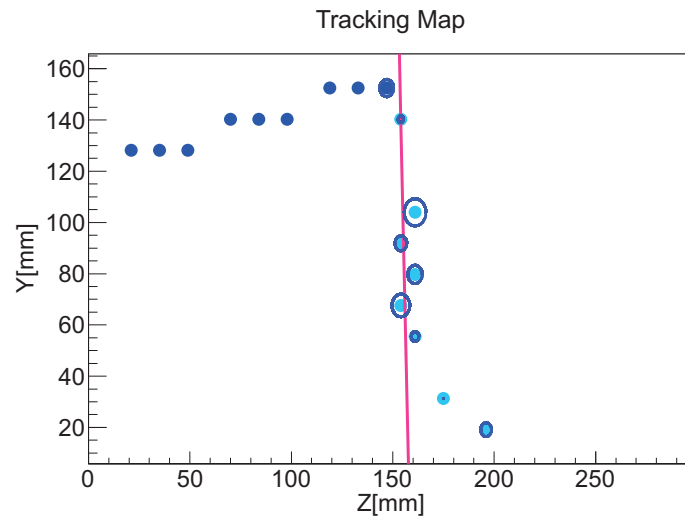


Figure 6.12: Tracking result with weight for the positron

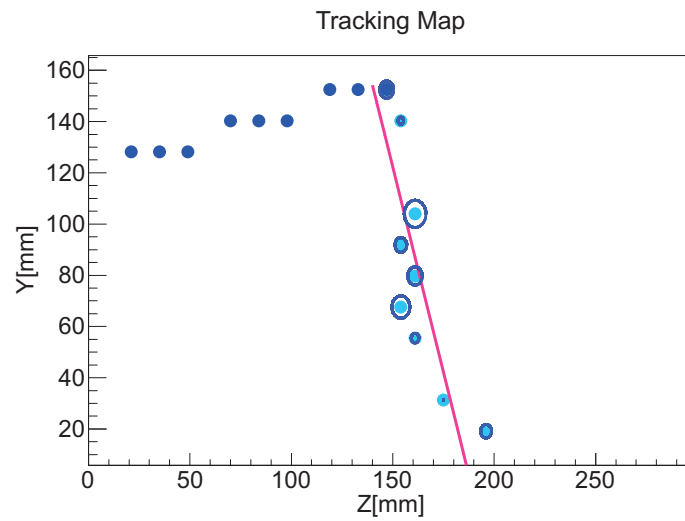


Figure 6.13: Tracking result without weight for the positron

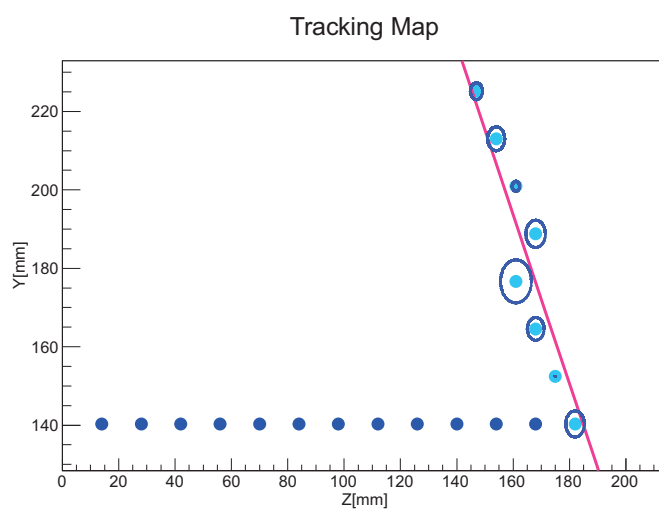


Figure 6.14: Another example of positron tracking

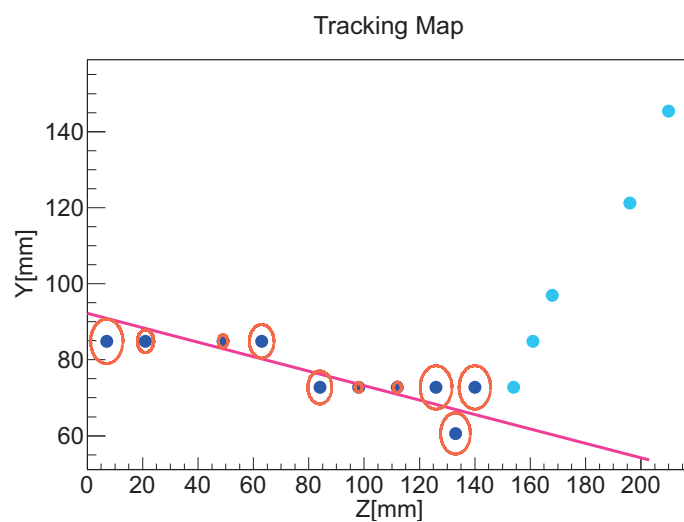


Figure 6.15: Incident muon tracking reconstruction fit

Using same fitting algorithm, I also reconstructed the incident muon tracking.

The tracking reconstruction efficiency was over 96% for the muons, for positrons the tracking efficiency was about 68% since it was difficult to fit the positron parallel to the wire for 2-dimension tracking. For 3-dimensional tracking, charge division method is required (Appendix B).

## 6.4 Asymmetry

Measuring the polarization by the MTP is an essential element of the TREK experiment, so the performance of the MTP must be known in advance. We used a polarized muon beam in our beam test, hence the MTP must measure the same longitudinal polarization and have null asymmetry in the transverse direction. As already mentioned in Section 5.4, the M11 muon beam is polarized in the forward direction, but it had not been clearly known since it had never been measured. Hence, the result of our  $\mu$ SR measurement was key to know the beam polarization.

### 6.4.1 Muon decay parameters

In the muon decay mode  $\mu \rightarrow e\nu\bar{\nu}$ , neglecting radiative corrections and the mass of the neutrinos and  $e^\pm$ , the differential decay probability can be written as

$$\begin{aligned} \frac{d^2\Gamma}{dx d\cos\theta} &\sim x^2 \cdot \left\{ 3(1-x) + \frac{2\rho}{3}(4x-3) + 3\eta x_0(1-x)/x \right. \\ &\quad \left. \pm P_\mu \cdot \xi \cdot \cos\theta \left[ 1-x + \frac{2\delta}{3}(4x-3) \right] \right\}. \end{aligned} \quad (6.9)$$

Here,  $\theta$  is the angle between the electron momentum and the muon spin, and  $x \equiv 2E_e/m_\mu$ .  $P_\mu = |\vec{P}_\mu|$  is the degree of muon polarization and  $x \equiv E_e/\max(E_e)$  is the reduced energy, where the maximum  $e^\pm$  energy,  $\max(E_e) = m_\mu/2 = 52.83\text{MeV}$ . The Michel parameters are bilinear combinations of the weak interaction coupling constants  $g_{e\mu}^\gamma$ . For the Standard Model coupling, the interaction corresponds to one single amplitude  $g_{LL}^V$  being unity and all others being zero, so  $\rho = \xi\delta = 3/4$ ,  $\xi = 1$ ,  $\eta = 0$  and the differential decay rate is

$$\frac{d^2\Gamma}{dx d\cos\theta} = \frac{G_F^2 m_\mu^5}{192\pi^3} [3 - 2x \pm P_\mu \cos\theta(2x-1)]x^2. \quad (6.10)$$

The antisymmetric part in  $\cos\theta$  represents the asymmetry, which depends on the  $e^\pm$  energy.

$$\frac{d^2\Gamma}{dx d\cos\theta} \sim F(x)[1 + \alpha(x)\cos\theta] \quad (6.11)$$

$$\alpha(x) = \pm P_\mu \frac{2x-1}{3-2x}. \quad (6.12)$$

The normalized symmetric part of the  $e^\pm$  energy spectrum has the form

$$F(x) = 2x^2(3-2x) \quad (6.13)$$

The decay distribution are shown Fig6.16 as a function of  $\cos\theta$  and  $x$ .

When the polarization of the  $\mu^\pm$  is 100%, the theoretical asymmetry averaged over all the possible  $e^\pm$  energies from  $x = 0$  to  $x = 1$  is given by,

$$\langle \alpha \rangle = \int_0^1 \alpha(x)F(x)dx = \pm \frac{1}{3}. \quad (6.14)$$

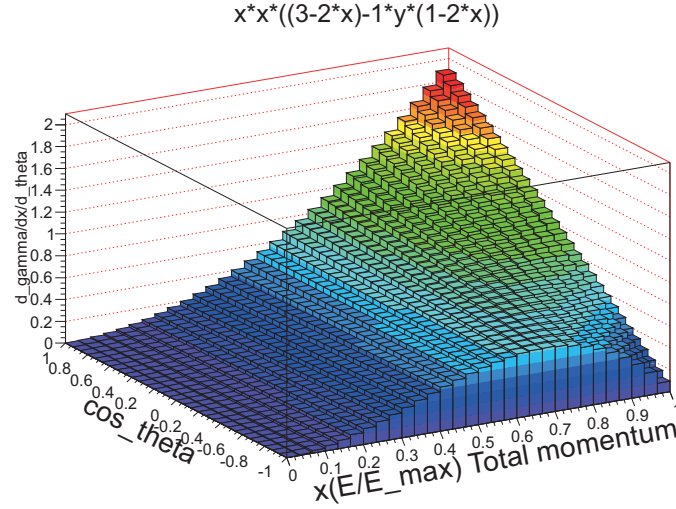


Figure 6.16: Distribution of decay positrons as a function of  $\cos \theta$  and  $x$

#### 6.4.2 Result of asymmetry measurement by the MTP

While a track is reconstructed by fitting as a straight line, I should pay attention to the fact that there were two possible direction for a line, the true direction and its opposite direction. I measured positron hit direction from the vertex. I will describe the selecting procedure.

When a line is expressed as  $az + by + c = 0$ , its directional vector is

$$u_1 = \left( -\frac{b}{\sqrt{a^2 + b^2}}, \frac{a}{\sqrt{a^2 + b^2}} \right) \quad (6.15)$$

or

$$u_2 = \left( \frac{b}{\sqrt{a^2 + b^2}}, -\frac{a}{\sqrt{a^2 + b^2}} \right). \quad (6.16)$$

The direction of average hit position with respect to the vertex can be expressed as;

$$p = (Z, Y) = \left( \frac{\sum_i^N x_i}{N} - z_{vertex}, \frac{\sum_i^N y_i}{N} - y_{vertex} \right). \quad (6.17)$$

Here,  $(z_i, y_i)$  is the positron hit wire position,  $N$  is the number of the positron hits,  $(z_{vertex}, y_{vertex})$  is the vertex position. The true angle can be selected requiring that the inner product  $u_1 \cdot p$  or  $u_2 \cdot p$  is positive and close to 1. And its  $x$  component  $\pm \frac{b}{\sqrt{a^2 + b^2}}$  means cosine. The events with cosine  $> 0$  means positron emitted in the forward, and cosine  $< 0$  means positron emitted in the backward direction. By counting those, asymmetry can be calculated.

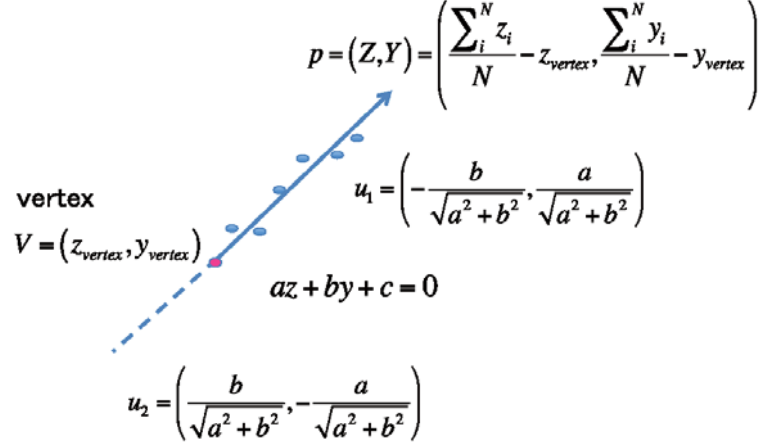


Figure 6.17: Schematic view of the tracking angle

Although I extracted clean tracks with no-bias before the main analysis, there remained a few bad events. When the selection was done ideally and the positron hit direction and line directional vector are the same, the opening angle of those vector  $\cos \psi = \frac{u_i \cdot p}{|u_i| |p|}$  ( $i = 1$  or  $2$ ) is expected to be close to 1. In fact, as seen Fig 6.18, there were event its  $\cos \psi$  close to 0, and example of those bad events, which could not be conducted tracking reconstruction, were shown in Fig 6.19.

In order to avoid using these bad events, I regarded events with an opening angle over 0.5 as good for the asymmetry calculation. In addition, although I selected the fiducial volume of the polarimeter including the vertex cell for a small region, I examined the systematics due to the size or position of the selection.

The asymmetry can be obtained as,

$$A_{f/b} = \frac{N_{fwd} - N_{bwd}}{N_{fwd} + N_{bwd}} \quad (6.18)$$

where a number of events with positrons  $N_{fwd}$  and  $N_{bwd}$  correspond to the  $z$  direction (*forward*) counts and the  $-z$  direction (*backward*) counts, respectively. where  $N_{fwd}$  and  $N_{bwd}$  correspond to the  $z$  direction (*forward*) and the  $-z$  direction (*backward*), respectively.

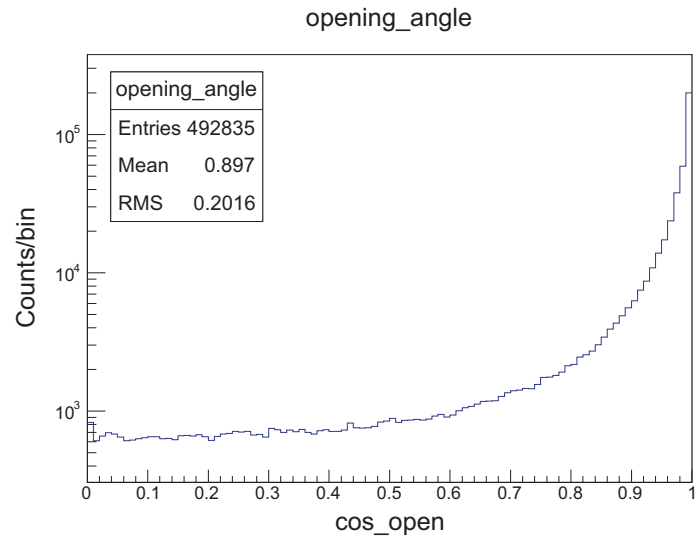


Figure 6.18: Opening angle distribution

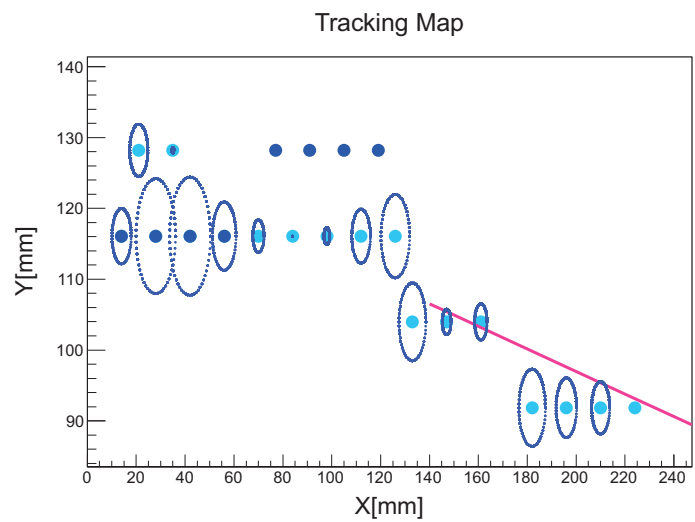


Figure 6.19: Example of bad events: Its opening angle is small, 0.387, because of there were two incident beam partially and the second beam mis-regarded as the positron, so the average of the positron hit was mis-calculated.

### 6.4.3 Systematics

It was simple if the MTP has no systematics. In fact, when I checked carefully, there seems to exist difficult systematics, then I studied how the details. In conclusion, with a finite size of a detector, a MTP, the problem seems unavoidable and the understanding is necessary. I describe and discuss the findings in this section.

Fig 6.20 and Fig 6.21 show the definition of emittance angles in three dimension and two dimension, respectively.

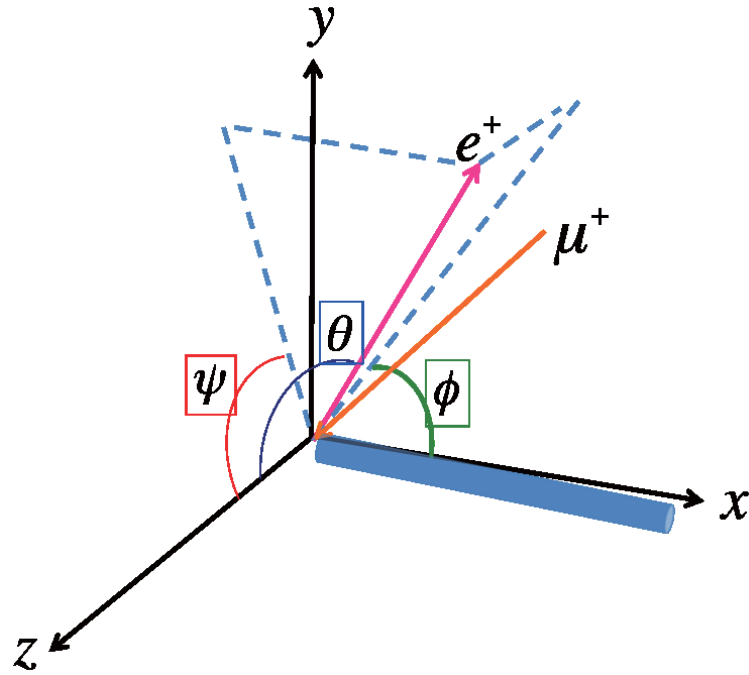


Figure 6.20: The coordinate system definition

The definition of the coordinate can be written as,

$$\begin{pmatrix} x \\ y \\ z \end{pmatrix} = \begin{pmatrix} \sin \theta \cos \phi \\ \sin \theta \sin \phi \\ \cos \theta \end{pmatrix} \quad (6.19)$$

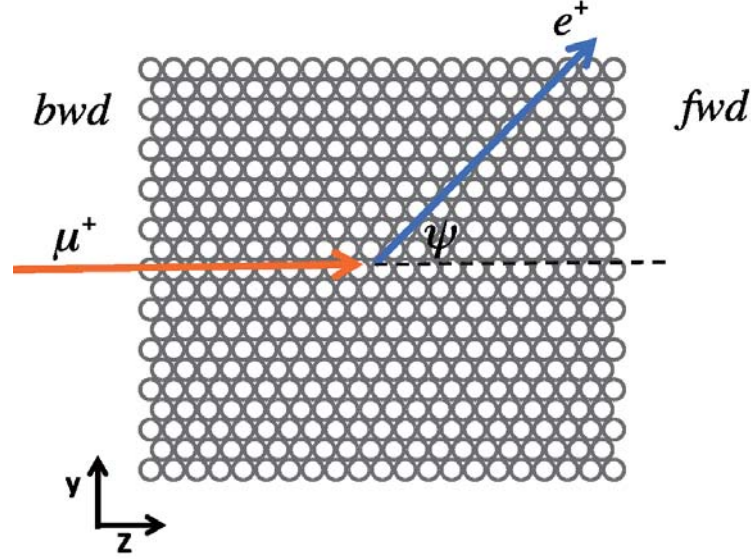


Figure 6.21: Schematic view of the muon decay for positron in the MTP

$$\cos \psi = \frac{z}{\sqrt{z^2 + y^2}} = \frac{\cos \theta}{\sqrt{\cos^2 \theta + (1 - \cos^2 \theta) \sin^2 \phi}}, \quad (6.20)$$

$$\sin \psi = \frac{y}{\sqrt{z^2 + y^2}} = \frac{\sin \theta \sin \phi}{\sqrt{\cos^2 \theta + (1 - \cos^2 \theta) \sin^2 \phi}}, \quad (6.21)$$

$$\theta = \arctan \left( \frac{\tan \psi}{\sin \phi} \right). \quad (6.22)$$

In the two dimensional tracking, we can see the projected angle  $\psi$ .

The number of events emitted *forward* or *backward* equivalent to the integral of  $\cos \psi > 0$  or  $\cos \psi < 0$ , respectively. Also, the number of events emitted *up* or *down* equivalent to the integral of  $\sin \psi > 0$  or  $\sin \psi < 0$ , respectively.

Using Eq 6.11 and Eq 6.20, without polarization, the  $\cos \psi$  distribution is expected to as Fig 6.22 and Fig 6.23.

Using the data analysis, in fact, these events whose positrons were emitted parallel to tube ( $x$ -axis) were difficult to two-dimensional tracking, these shape of  $\cos \psi$  distribution and  $\sin \psi$  distribution should be deformed. Fig 6.24 and Fig 6.25 shows simulation by Geant4.

## Data

Although the asymmetry measured by the MTP seems to be obtained simply, there exists systematics depending on the incident particle stopping position of the

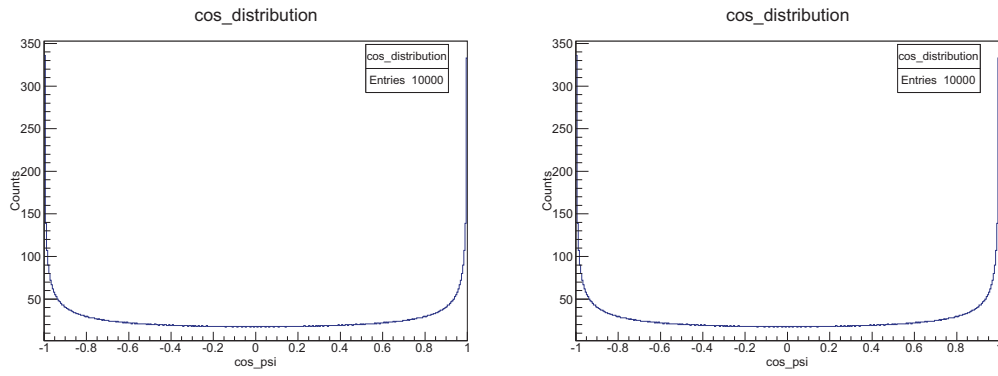


Figure 6.22:  $\cos \psi$  by analytic calculation Figure 6.23:  $\sin \psi$  by analytic calculation

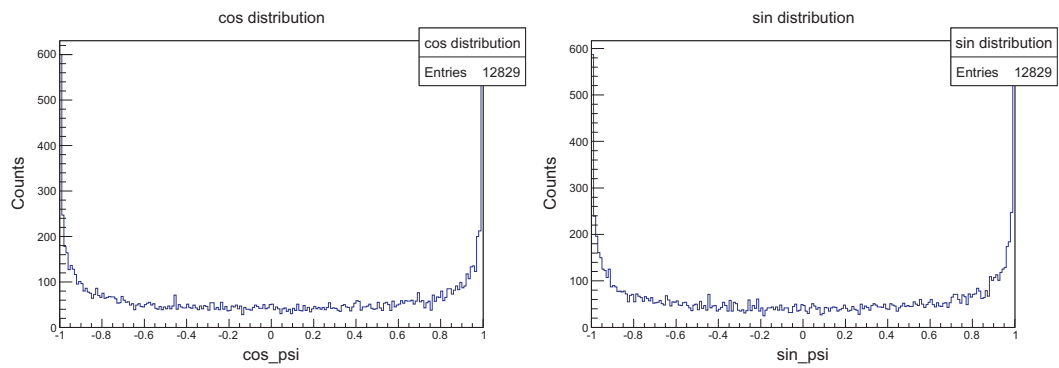


Figure 6.24:  $\cos \psi$  generated by Geant4 simulation Figure 6.25:  $\sin \psi$  generated by Geant4 simulation

fiducial volume. Fig 6.26 shows the definition of the fiducial volume. I divided fiducial middle of MTP area into four fiducial volume, a to d.

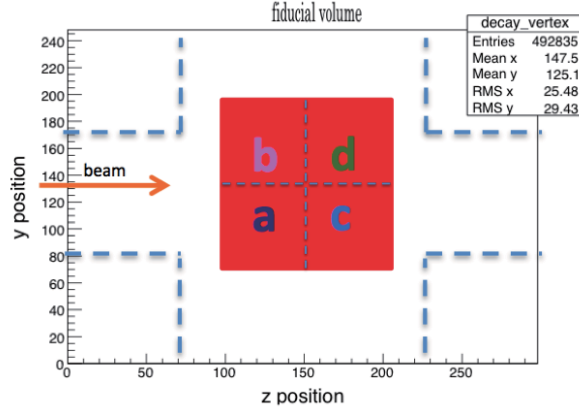


Figure 6.26: Definition of the fiducial volume. The area in the dashed line means the read-out region.

- $\mu^+ \rightarrow e^+ \nu_\mu \nu_e$  data

According to Fig 6.27 and Fig 6.28, the distributions has some structure peak corresponding to 0 degree, 30 degree, and 60 degree. I think this comes from two dimension tracking and the filling structure of tube in the MTP.

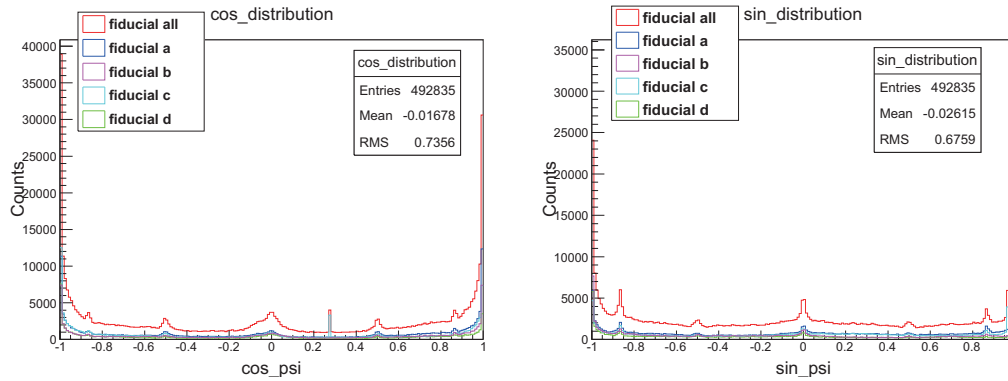


Figure 6.27:  $\cos \psi$  distribution of the muon data

Figure 6.28:  $\sin \psi$  distribution of the muon data

The measured asymmetry is not uniform depends on the fiducial volume (Fig 6.29, Fig 6.30). In case of the forward or backward asymmetry, it is different the forward area (c and d) and the backward area (a and b) in Fig 6.29. Also, in case of the up or down asymmetry, it is different with the

upward area (b and d) and the downward area (a and c) in Fig 6.30. This should be comes from the MTP has a finite size.

It is not understood why the asymmetry depends on the opening angle cut. The opening angle cosine nearly one means the fitting direction and the average of the positron hitting direction are the almost same.

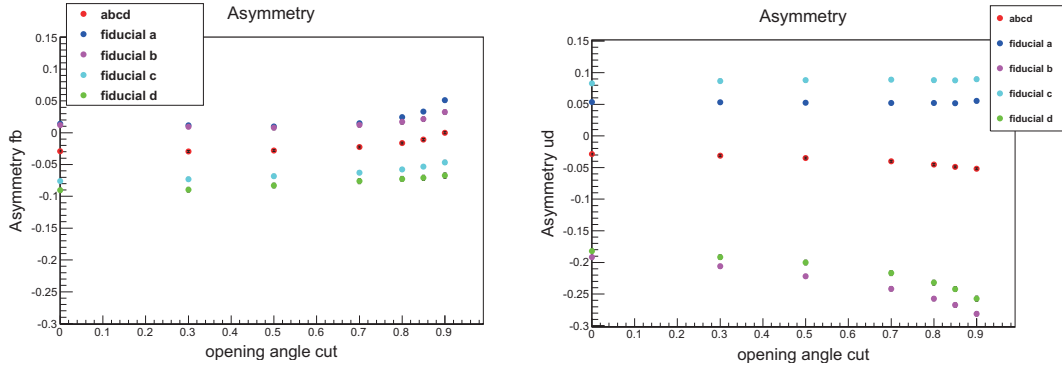


Figure 6.29: *Forward* or *backward* asymmetry of the muon data

Figure 6.30: *Up* or *down* asymmetry of the muon data

- $\pi^+ \rightarrow \mu^+ \nu_\mu$ ,  $\mu^+ \rightarrow e^+ \nu_e$  data

Since the spin of pion is 0, the emission angle of muon from decays of stopped pion is expected to be isotropic, therefore no asymmetry of positrons are expected. However asymmetries are observed also in the pion data. (Fig 6.31, Fig 6.32 and Fig 6.33, Fig 6.34).

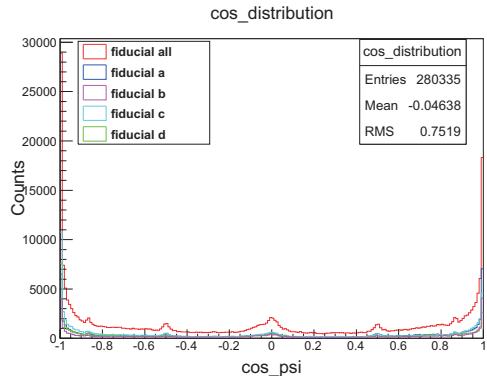


Figure 6.31:  $\cos \psi$  distribution of the pion data

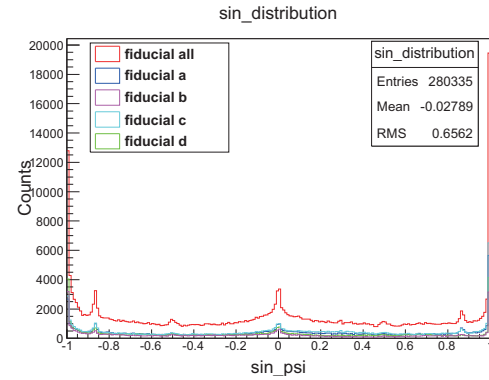


Figure 6.32:  $\sin \psi$  distribution of the pion data

The behavior of the muon and the pion data are similar, so there must be common systematic effects with the MTP.

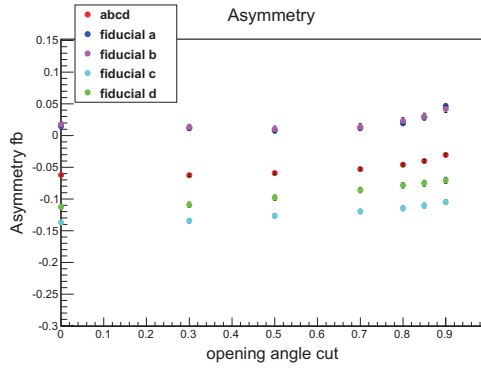


Figure 6.33: *Forward* or *backward* asymmetry of the pion data

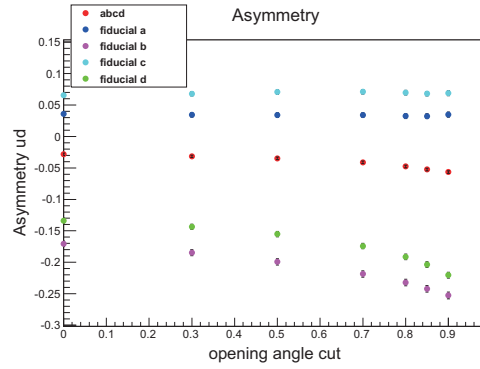


Figure 6.34: *Up* or *down* asymmetry of the pion data

### More smaller fiducial volume

I defined the more smaller fiducial volume. Fig 6.35 shows the new definition of the fiducial volume. I also divided fiducial middle of MTP area into four fiducial volume, a to d.

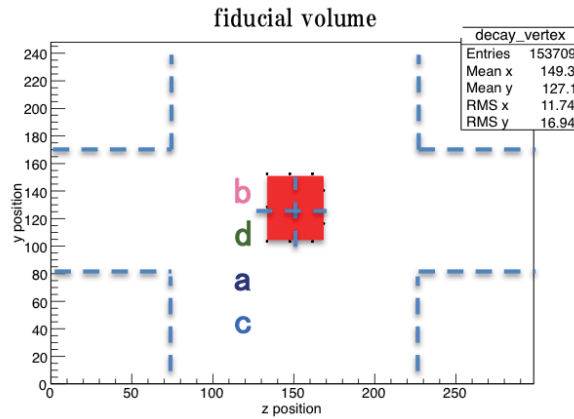


Figure 6.35: Definition of the fiducial volume

- $\mu^+ \rightarrow e^+\nu_\mu\nu_e$  data

There seems the same position dependency (Fig 6.36, Fig 6.37 and Fig 6.38, Fig 6.39).

- $\pi^+ \rightarrow \mu^+\nu_\mu$ ,  $\mu^+ \rightarrow e^+\nu\bar{\nu}$  data

There also seems the asymmetry (Fig 6.40, Fig 6.41 and Fig 6.42, Fig 6.43).

The behavior of the muon and the pion data are also similar. The difference of both of their *fwd/bwd* asymmetry are small these results, the *up/down*

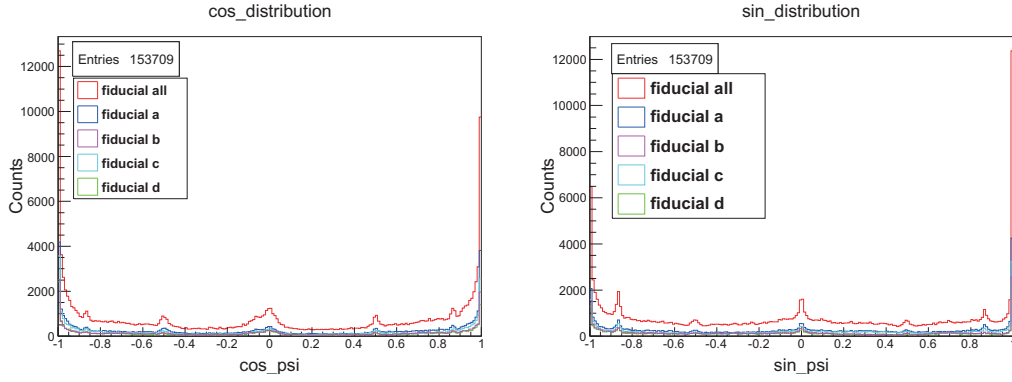


Figure 6.36:  $\cos\psi$  distribution of the muon data with small fiducial volume

Figure 6.37:  $\sin\psi$  distribution of the muon data with small fiducial volume

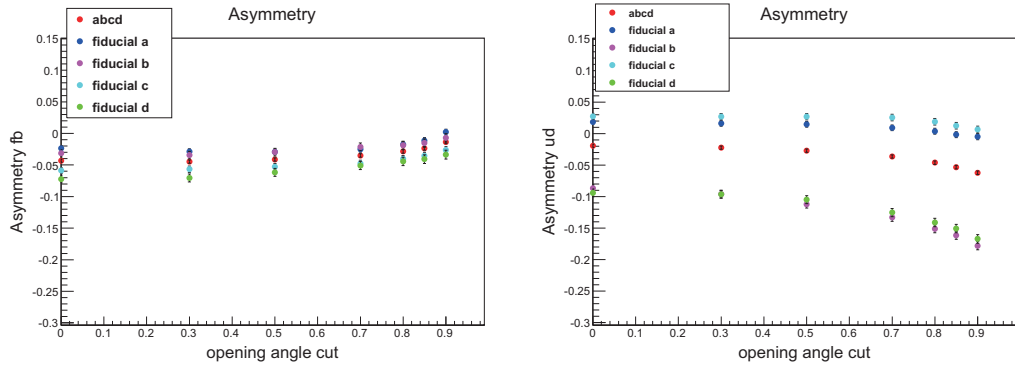


Figure 6.38: Forward or backward asymmetry of the muon data with small fiducial volume

Figure 6.39: Up or down asymmetry of the muon data with small fiducial volume

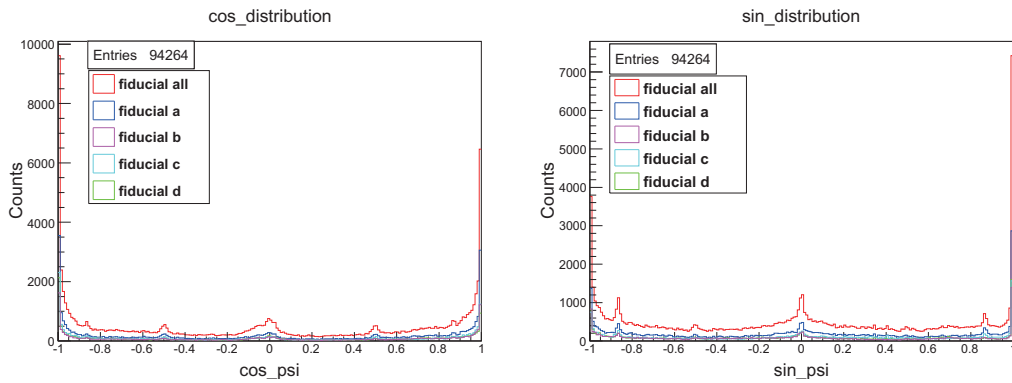


Figure 6.40:  $\cos\psi$  distribution of the pion data with small fiducial volume

Figure 6.41:  $\sin\psi$  distribution of the pion data with small fiducial volume

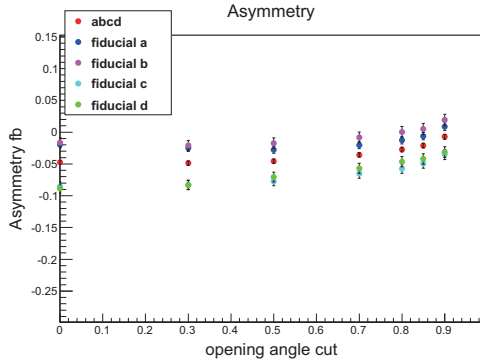


Figure 6.42: *Forward or backward* asymmetry of the pion data with small fiducial volume

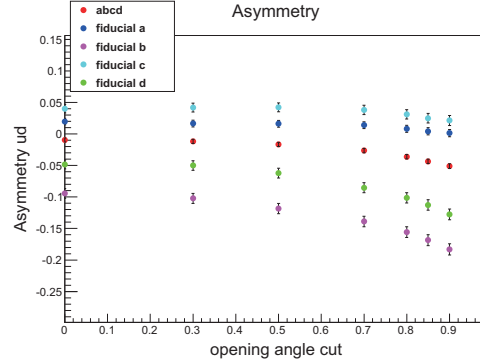


Figure 6.43: *Up or down* asymmetry of the pion data with small fiducial volume

asymmetry are not so improved. The length of the vertical direction is shorter than front-back direction, so this might be have some relation.

#### 6.4.4 Muon incident angle

I checked the incident beam angle distributions with muons. Although we set the beam incident parallel to  $z$ -axis, some muons yield to incide obliquely. Fig 6.44 and Fig 6.45 shows the results of the tracking reconstruction  $\cos\psi$  distribution and  $\sin\psi$  distribution which contains some bad fitting and the results of fitting  $\chi^2/NDF$  value distribution, respectively (here,  $NDF$  (= number of degree of freedom) is fitting parameter(4) - 1. The time starting point  $t_0$  of muons could be known.). There exists large  $\chi^2/NDF$  value, hence I used the only good,  $\chi^2/NDF < 20$  events. Then I got expecting shape of the muon incident angle distribution, Fig 6.46. The RMS of distribution of 130 mrad, which was adequate the effect of both the multiple scattering in the degrader ( $\sim 94$  mrad) that is 94mrad for 170 MeV/c muons and the beam expansion ( $\sim 33$  mrad).

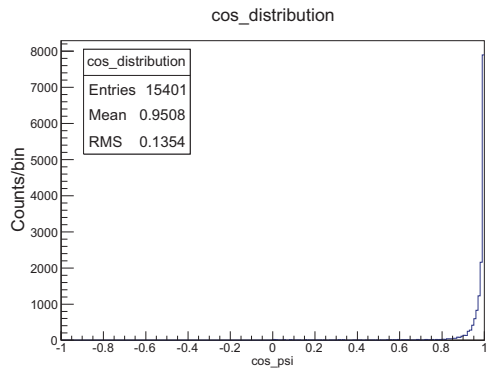
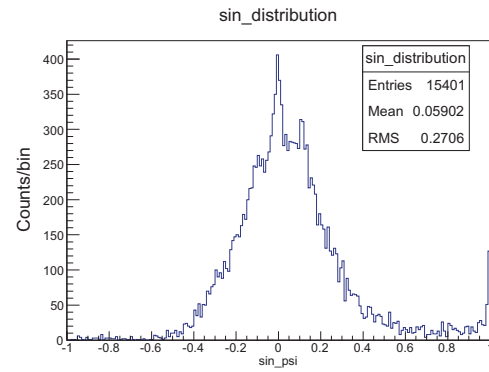
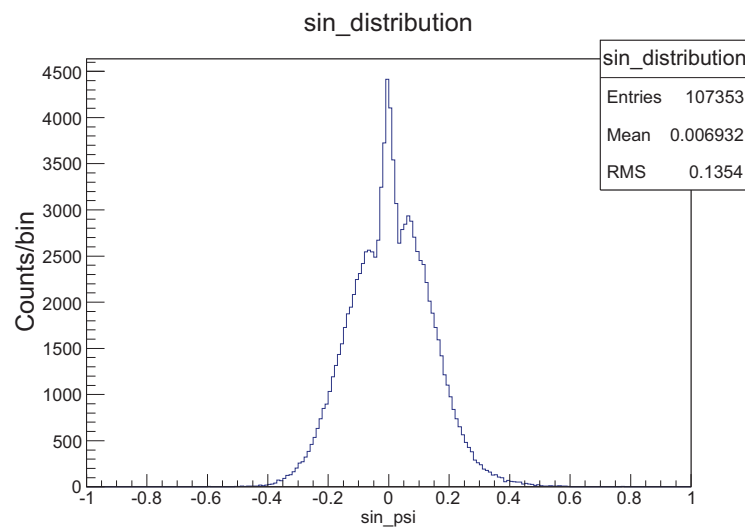
And the structure of the three peaks may come from left right ambiguity of tracking reconstruction.

## 6.5 Analyzing Power

When results of asymmetry from both the  $\mu$ SR measurement and the MTP measurement are obtained, the analyzing power, which is characteristic value of the MTP itself, can be obtained.

The analyzing power of the MTP is defined as

$$\alpha = A_{f/b}/P_{\mu}. \quad (6.23)$$

Figure 6.44: no cut  $\cos \psi$ Figure 6.45: no cut  $\sin \psi$ Figure 6.46: After cut of  $\chi^2/NDF < 20$   $\sin \psi$  distribution

where,  $A_{f/b}$  is the *forward* or *backward* asymmetry, and  $P_\mu$  is the beam polarization.

## 6.6 More detailed analysis

A number of systematic effects have been observed in the data analysis. For better understanding and further research, the followings should be done:

- Detailed Monte Carlo simulation  
By comparing the true track and the reconstruction track, we can estimate the systematic errors.
- 3-dimensional tracking  
I reconstructed 2-dimensional tracking algorithm, but in fact, muons decay in 3-dimension space hence the x-direction dependence should be known in final. With the charge division method, I refer precisely in Appendix B, the position of the hit in the x-direction can be known by comparing the charge quantity of both sides of the readout. The combination of 2-dimensional tracking and charge division can provide mean 3-dimensional tracking.
- Efficiency estimation by track reconstruction
- Improvement of tracking reconstruction

In addition, improvement of ASB cards design is desirable. During the beamtest, there was a strange peak in the lower channels of the ADC spectrum due to the problem with the ASB cards. Fortunately, we had no bad effect by changing the ADC threshold. However, for charge division study, the correlation between both sides of readout was important, so we couldn't use the lower channels.



## Chapter 7

# Conclusion

The TREK aims to measure the transverse polarization  $P_T$  in  $K_{\mu 3}$  decay with accuracy  $\delta P_T < 10^{-4}$ , using upgraded E246 detector. There are two choice for the TREK polarimeter, a plate type or a tube type (MTP).

We had beam test in order to evaluate the performance of the MTP. We tuned beam condition and determined the degrader thickness. The beam polarization we used had not been known, so we measured by means of  $\mu$ SR. We had a result that the beam polarization of M11 muon beam at 170 MeV had about 17% backward polarization.

I studied the basical MTP performance. The wire efficiency was good enough (>99%), and the efficiency depended on drift distance was also high enough. I estimated the drift velocity by fitting the drift time distribution. I cross checked the estimation by the X-T relation. Using the drift velocity, I made tracking reconstruction algorithm considering the multiple scattering.

It is desirable that there exists few systematics in the MTP. However, I found some systematics in the MTP, so further examination is needed.



# Appendix A

## Beam tuning at J-PARC K1.1BR

The J-PARC (Japan Proton Accelerator Research Complex) consists of a series of world-class proton accelerators and experimental facilities that make use of the high-intensity proton beams.

J-PARC K1.1BR at the Hadron hall is one of the beam channels of the J-PARC Hadron Experimental Hall and the TREK is planned to in this area. In the TREK experiment, we will use a separated  $K^+$  beam with 0.8 GeV/c momentum from K1.1BR. The K1.1BR beamline with a total length of 21.5 m was made as a branch beamline of K1.1, namely the K1.1BR uses the upstream magnets (from  $D1$  to  $MS$ ) of K1.1. The design intensity proton beam (50 GeV, 15  $\mu$ A, 750 kW), guiding T1 target, using secondary particle for various atomic or particle experiments. The momentum is about 740 MeV/c to 800 MeV/c, and expected beam intensity is about  $3 \times 10^4 K^+ / spill$  when first beam line intensity is 2kW.

We are planning the following two precision measurements using the stopped  $K^+$  beam at K1.1BR.

- E36: Measurement of  $\Gamma(K^+ \rightarrow e^+\nu)/\Gamma(K^+ \rightarrow \mu^+\nu)$  and search for heavy sterile neutrino using the TREK detector system
- E06(TREK): Measurement of T-violating Transverse Muon Polarization in  $K^+ \rightarrow \pi^0\mu^+\nu$  decays

The beam optics of K1.1BR[ , ] was designed by J.Doornbos of the TREK collaboration. In the design of the beamline, it is essential to increase the  $K/\pi$  ratio higher than 2 and the kaon yield as much as possible in order to satisfy the TREK requirement.

The detector elements and the beam optics for the K1.1BR beamline(Fig A.4) are the following.

- Proton target ( $T1$ ) and first bending magnet ( $D1$ )
- Quadrupole doublet  $Q1 - Q2$  and intermediate vertical focus ( $IFY$ )

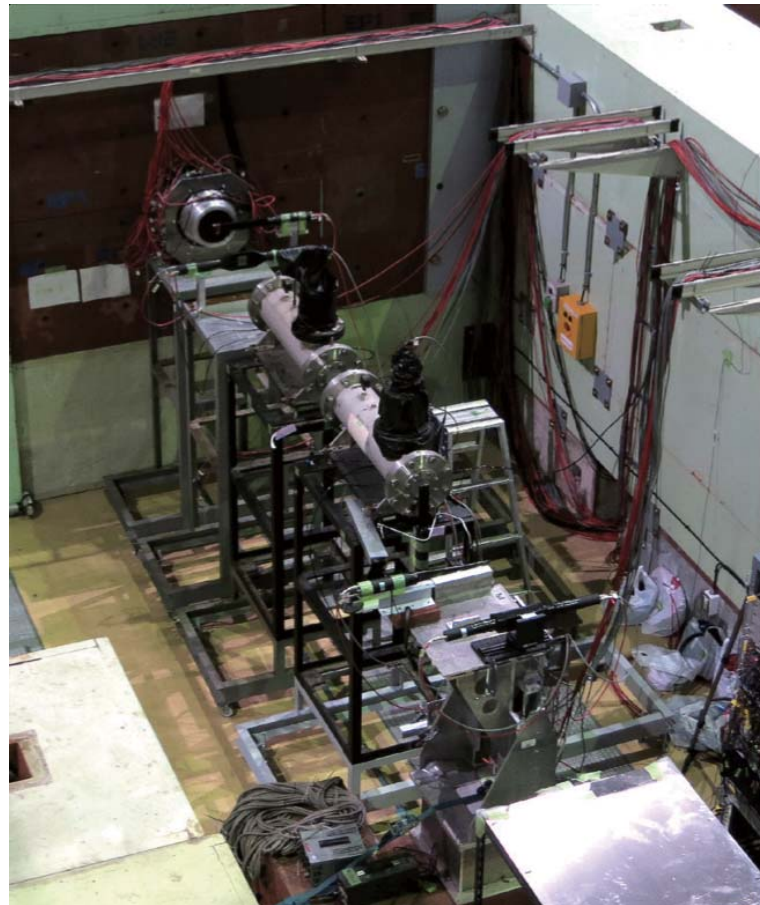


Figure A.2: Detectors for beam measurement

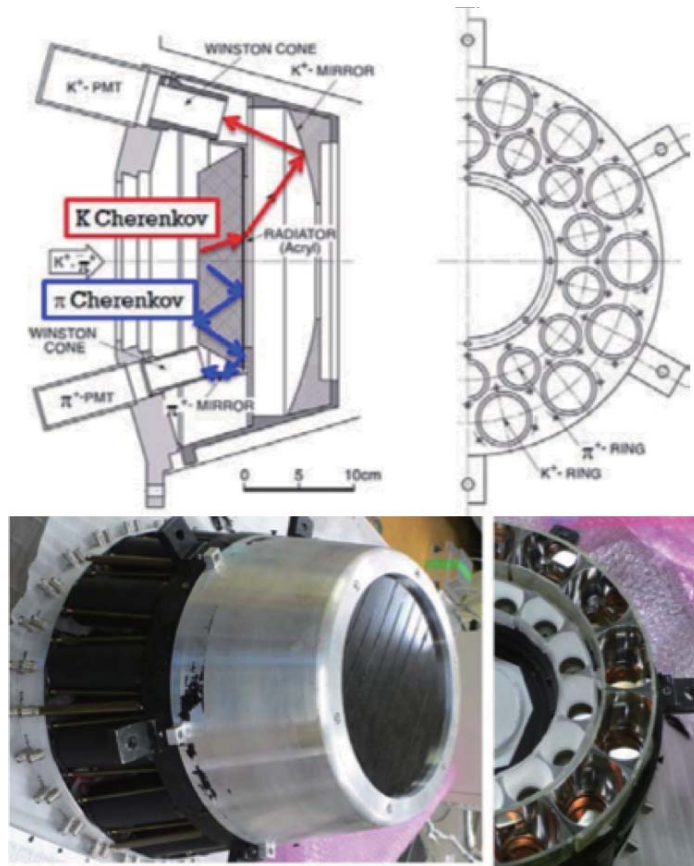


Figure A.3:  $\pi/K$  differential Fitch-type Čerenkov counter

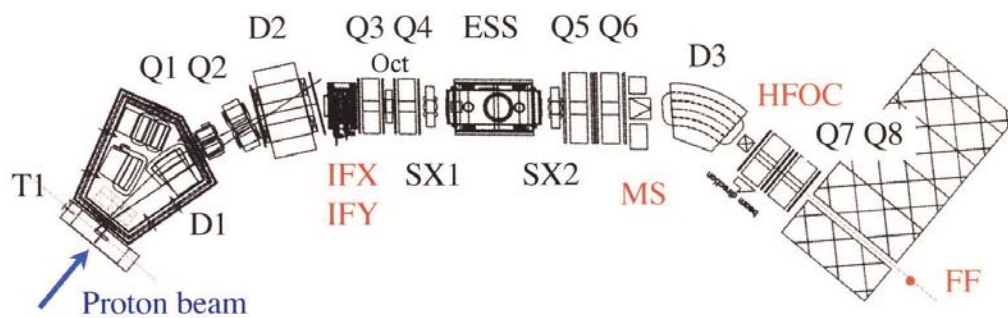


Figure A.4: The layout of K1.1BR beamline

- Quadrupole doublet  $Q3 - Q4$  and the electrostatic separator ( $ESS$ )
- Quadrupole doublet  $Q5 - Q6$  and mass slit ( $MS$ )
- The final bending magnet ( $D3$ )
- Quadrupole doublet  $Q7 - Q8$  and horizontal focus ( $HFOC$ )
- Sextupole magnets ( $SX1$  and  $SX2$ ) and octupole magnet(01)

We conducted beam tuning from May 2012 to June 2012, and re-tuned the  $K^+$  beam for good condition. We determined that the condition of the beam and magnets were recovered from autumn 2010, when TREK had beam tuning before the big earthquake of March 2011. In addition, we measured excellent  $K^+$  beam acceptance which is large enough for E06 and E36 under the expected  $K/\pi$  ratio with wide slit. The detectors used for beam measurement were the following:

- Hodoscope : beam profile measurement
- Fitch Čerenkov :  $K/\pi$  identification (Fig A.3)
- Beam defining counter : trigger
- TOF1 and TOF2 :  $K/\pi$  identification
- Gas Čerenkov : positron identification (veto for  $e^+$ )

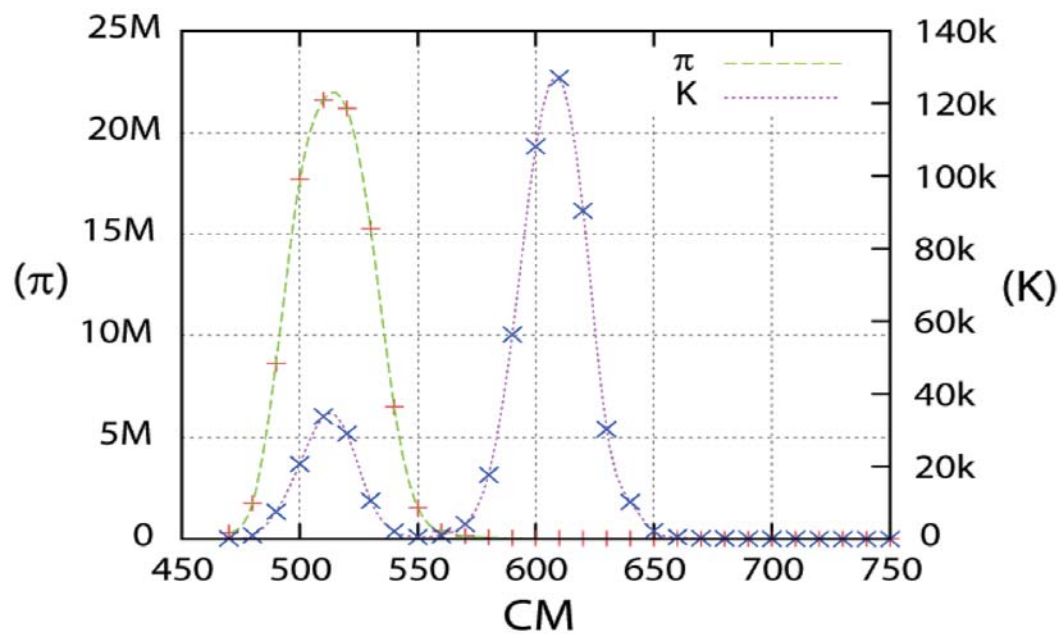


Figure A.5: Results of  $K^+/\pi^+$  separation curve using narrow slit



# Appendix B

## Charge division

Following is the briefly description of the mechanism of the charge division method. As shown in Fig B.1, the distance between particle hit position and the wire ends are defined as  $Z_1$  and  $Z_2$ , and the resistances corresponding to the distances are defined as  $R_1$  and  $R_2$ , respectively. In addition to these wire resistances we have to consider

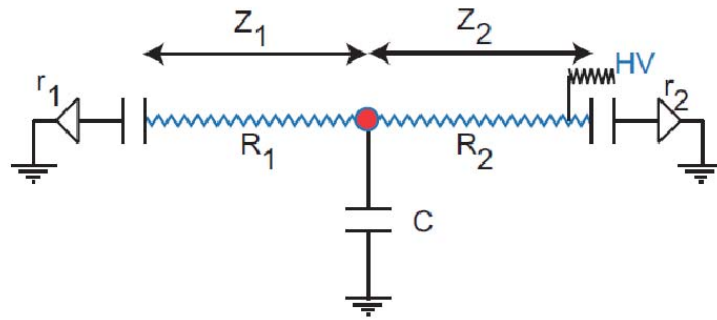


Figure B.:2: The schematic view of charge division system.

the input impedance of amplifiers, which are defined as  $r_1$  and  $r_2$ , respectively. In this case, the equivalent circuit can be expressed as shown in Fig B.2.

The collected charge on the virtual capacitance is discharged through the resistance. The experimentally time-integrated  $I_1$  and  $I_2$  currents are observed as the charges  $Q_1$  and  $Q_2$ , respectively. Using the capacitance  $C$  and voltage  $V$ , the

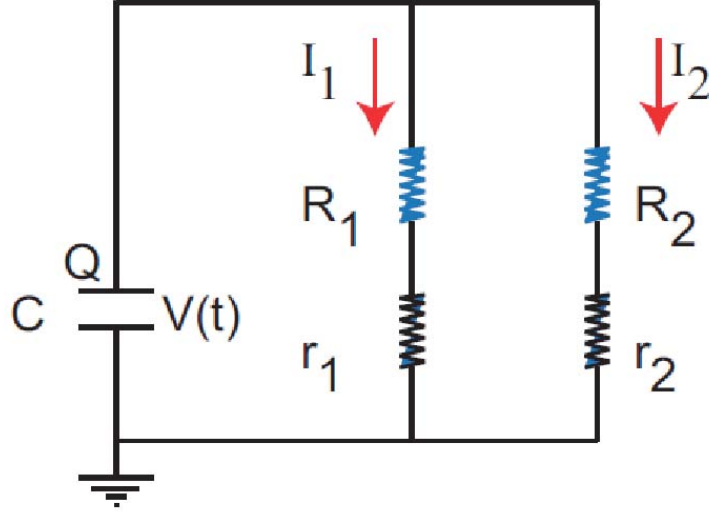


Figure B.:3: The equivalent electric circuit of the charge division system.

charge  $Q$  can be written as,

$$V = I_1(R_1 + r_1) = I_2(R_2 + r_2), \quad (\text{B.2})$$

$$Q = \int (-I)dt = CV, -I = -(I_1 + I_2) = C \frac{dV}{dt}, \quad (\text{B.3})$$

thus,

$$C \frac{dV}{dt} = -\frac{V}{R_1 + r_1} - \frac{V}{R_2 + r_2} = -\left( \frac{1}{R_1 + r_1} + \frac{1}{R_2 + r_2} \right) V, \\ V = -\frac{(R_1 + r_1)(R_2 + r_2)}{R_1 + R_2 + r_1 + r_2} C \frac{dV}{dt} = -r \frac{dV}{dt} \quad (\text{B.4})$$

$V$  can be obtained as

$$V(t) = V(0) \exp(-t/\tau) \quad (\text{B.5})$$

and

$$I_1 = \frac{1}{R_1 + r_1} \frac{Q}{C} \exp(-t/\tau) \\ I_2 = \frac{1}{R_2 + r_2} \frac{Q}{C} \exp(-t/\tau). \quad (\text{B.6})$$

The charges of both ends wire are obtained by time-integration of  $I_1$  and  $I_2$  as

$$Q_1 = \int (-I_1)dt = \frac{1}{R_1 + r_1} \frac{Q}{C} \tau = \frac{R_2 + r_2}{R_1 + R_2 + r_1 + r_2} Q, \\ Q_2 = \int (-I_2)dt = \frac{1}{R_2 + r_2} \frac{Q}{C} \tau = \frac{R_1 + r_1}{R_1 + R_2 + r_1 + r_2} Q. \quad (\text{B.7})$$

From the relation of

$$\frac{Z_1}{Z_2} = \frac{R_1}{R_2}, \quad (\text{B.8})$$

$Q_1/Q_2$  can be described by using  $Q = Q_1 + Q_2$ ,  $R = R_1 + R_2$ , and  $Z = Z_1 + Z_2$  as,

$$\frac{Q_1}{Q_2} = \frac{R_2 + r_2}{R_1 + R_2 + r_1 + r_2} = \frac{R_2/R + r_2/R}{1 + (r_1 + r_2)/R} = \frac{Z_2/Z + r_2/R}{1 + (r_1 + r_2)/R}. \quad (\text{B.9})$$

Therefore, the particle hit positions can be determined by the output charges from both wire ends as,

$$\begin{aligned} \frac{Z_1}{Z_2} &= \left(1 + \frac{r_1 + r_2}{R}\right) \frac{Q_1}{Q} - \frac{r_2}{R}, \\ \frac{Z_1}{Z_2} &= 1 - \frac{Z_2}{Z} = \left(1 + \frac{r_1 + r_2}{R}\right) \frac{Q_2}{Q} - \frac{r_1}{R}, \\ \frac{Z_1 - Z_2}{Z} &= \left(1 + \frac{r_1 + r_2}{R}\right) \frac{Q_1 - Q_2}{Q} - \frac{r_1 - r_2}{R}. \end{aligned} \quad (\text{B.10})$$

In the coordinates where  $x$  is the distance of the particle hit position from the center ( $x = 0$  is center),  $x$  is written as,

$$\frac{x}{Z} = \left(1 + \frac{r_1 + r_2}{R}\right) \frac{Q_1 - Q_2}{2Q} - \frac{r_1 - r_2}{2R}, \quad (\text{B.11})$$

where  $Z_1 - Z_2 = 2x$ .



# Appendix C

## Tracking system for the TREK detector

With the upgraded of the tracking system of TREK detector, the error from background  $K_{\pi 2}^+ - dif$  will be improved to meet the requirement of  $< 10^{-4}$  for the total systematic error in  $P_T$ . These performance goals will be achieved both by reducing the material budget along the track and by rearranging existing and adding new tracking elements in replacement of the previous C1 chamber. The momentum uncertainty of 3.6MeV/c in E246 can be reduced by at least a factor of 10

1. by employing a 6-cm- instead of 9.3-cm-wide target with a segmentation of  $3.0 \times 3.0 mm^2$  fibers instead of  $5 \times 5 mm^2$
2. by replacing the air volume in the magnet between C2 and C3 and before C2 chambers with helium bags
3. by increasing the distance between the C3 and C4 elements to 30cm from 15cm.

For sufficient identification and suppression of  $K_{\pi 2}^+ - dif$  events we need to build a cylindrical tracking chamber ("C0") with a radius of 10cm and a spatial resolution of  $< 0.1mm$ . The new C0 chamber will replace the previous cylindrical C1 chamber of the E246 setup. In order to increase tracking redundancy we propose to add new planar element (again named "C1") with  $< 0.1mm$  resolution to cover each of the 12 gaps at the outer surface of the CsI(Tl) calorimeter. By adding these additional elements to the tracks which do not have a kink along their path. In combination with the higher segmentation of the fiber target this will be sufficient to suppress the  $K_{\pi 2}^+ - dif / K_{\mu 3}^+$  ratio below  $10^{-3}$ , rendering a spurious  $P_T < 5 \times 10^{-5}$ .

The planned modifications are in summery:

1. Thinner target with higher segmentation.
2. Helium gas bags in the magnet between C2 and C3, and before C2.
3. Increase in the distance between C3 and C4 to 30cm from 15 cm.

4. Addition of new tracking elements: "C0" and "C1" chambers based on GEM technology.

Fig7 and tableC.2 show comparisons of the tracking system in E246 and the TREK experiment. The GEM technology on which both C0 and C1 will be based presents a new generation of positron-sensitive counters that are reasonably cheap, radiation hard, and well suited to be operated in high-rate environments.

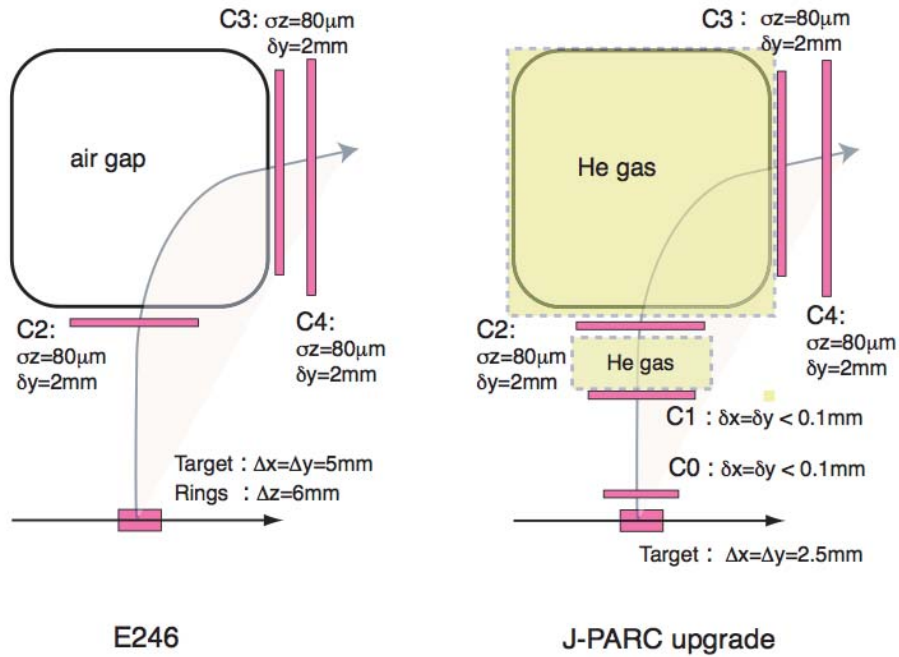


Figure C.2: Schematics of the tracking system in the TREK setup (*right*) compared with that of the E246 experiment (*left*).

Table C.2: Main parameters of the charged particle tracking.

Item	E246	TREK
High-resolution elements	C2, C3, and C4	
Target fiber	5×5mm + rings	3×3mm
C0 chamber	MWDC	Cylindrical GEM
C1 chamber		Plannar GEM chamber
C2 chamber	MWPC	MWPC (not charged)
C3 chamber	MWPC	MWPC (not charged)
C4 chamber	MWPC	MWPC (not charged)
C3-C4 distance	15cm	30cm
Magnet gap	Air	He gas bag
Total material thickness	$\sim 7 \times 10^{-3} X_0$	$6.6 \times 10^{-3} X_0$



# Appendix D

## Read-out system for the polarimeter beam tests

The main data acquisition stream for the MTP follows below. First of all, the MTP raw signals are input into an ASB card. The ASB card serves as Amplifier(A), shaper(S), and buffer(B). The ASB output signal passes through a flat cable and is input to a VME-discriminator board which requires about  $\pm 5V$  for its operation. The VME-discriminator board works as an ordinary discriminator, and has three kinds of outputs which are an analog signal and two logic signals, a LVDS and a NIM signal. The analog signal and the LVDS signal are required for the CAEN ADC and TDC modules. On the other hand, the NIM signal is used in order to tag the MTP signals. The trigger logic includes the NIM output signals. After the VME-discriminator board, the LVDS signals are input into the CAEN TDC modules. The TDC modules are used to take both MTP data and all scintillation counters. In terms of impedance matching for the ADC modules, a De-coupler card was also required for our measurement. The De-coupler cards are connected directly to the CAEN ADC modules for the adoption of the charge division method. The important parts of the data acquisition system are summarized in next sections.

### 16ch Amp. Shaper Buffer card

Special ASB IC (JRK-ASB(N)-1) chips were developed by the KEK electronics shop and the REPIC Co. The standard Amp. Shaper Discriminator (ASD) card is unsuited for the charge division method. Basically, an analog input signal from an anode wire is integrated for all 16 channels on one board with a 25 ns time constant. In addition, the output signal pulse height can be changed using the gain controller. The ASB has a small input impedance, thus, it is possible to adopt it to the charge division method. The main functions are summarized in Table D.2.

Table D.2: The main functions of ASB

ASB IC	JRK-ASB(N)-001 $\times$ 4 pcs
Analog input	negative charge input / 16 ch input
Maximum quantity of charge	1.5 pC with minimum gain
Shaping time constant	about 25 ns
Test input	negative NIM 50 $\Omega$ impedance
Analog output	- 3.75 V $\sim$ - 1.25 V
Vth control	$\leq$ + 2.5 V
Digital output	ECL output
Consumption of electricity	+ 5 V 500 mA / - 5 V 300 mA

### VME discriminator board MODEL RPV-240

The VME discriminator boards have not only analog outputs but also LVDS outputs. The former signals are used for the ADC and the latter ones are used for the TDC. The discriminator modules have a function of adjusting the threshold level, it is necessary to provide a DC signal level ( $\leq$  5 V) from an external DC power supply. In addition, this module produces a NIM signal, which is generated as an OR output even if only one of the 16 channels has a hit. The main specifications are summarized in Table D.3.

Table D.3: The specs of VME discriminator board

INPUT	16 CH Analog INPUT
Vth INPUT	Maximum INPUT 5 V
Analog OUTPUT	16 CH Analog OUTPUT
Digital OUTPUT	16 CH Digital OUTPUT (LVDS 110 $\Omega$ )
OR OUTPUT	16 CH OR OUTPUT (Negative NIM 50 $\Omega$ impedance)
POWER SUPPLY	+ 5 V / 1.1 A

### De-coupler card

The De-coupler card works as an attenuator. In order to take ADC data, the output signals must have 3 times lower pulse height than the signal input by the VME discriminator when it exceeds 1V. Actually, the quantity of the integrated charge is limited to the CAEN ADC's dynamic range. So as to achieve a higher position resolution along the wire direction, it is necessary to gain a lot of charge before the pulse shaping by the ASB card. At the same time, the quantity of charge has to be reduced to be able to take ADC data. Furthermore, the De-coupler card also works as a 200 ns delay module. As the trigger timing is always delayed by more than 100 ns compared to the time reference, delaying the analog signals is also necessary for

ADC data taking. As mentioned above, the De-coupler card plays an important role for the analog signals.

### **CAEN QDC V792 / CAEN TDC V1190**

The CAEN ADC V792 and CAEN TDC V1190 modules were used for the data acquisition. An ADC module has 32 channels and provides the time data for the charge division method, and a TDC module has 64 channels and provides data for drift time measurement. In case a wire is hit two or more times on one event, a multi-hit TDC module is required so that one channel can take more than 2 data hits for each event. This means that both the muon and the positron can pass near the same wire. This requirement is met by using the CAEN TDC V1190. The ADC is not multi-hit, thus we could take just the positron ADC data which was essential to measure the positron along the wire using the charge division method. Instead a FADC will be used for the MTP data acquisition in the TREK experiment, so it will be possible to collect both ADC and TDC data for both the muons and the positrons.



# Acknowledgements

I would like to express my sincere thankfulness to my supervisor, Prof. Tatsuo Kawamoto for continuously encouraging and supported the whole of my study. He gave so many helpful advice, and a lot of discussions with him including daily conversations greatly attracted me to particle physics so much. I would like to express my gratitude to Prof. J. Imazato, who gave me so many chances to learn a lot about physics through this exciting experiments. I have acquired an attitude to a physicist from him. I would like to thanks Prof. S. Asai, who allowed me to join this experiment. I deeply appreciate Dr. T. Namba for his valuable suggestions and support. I am extremely grateful for Prof. M. Hasinoff for carefully reading this thesis, and also for teaching me to how to tune the beam at TRIUMF. His vivid personality always get rid of my fatigue during the hard beam time. I would like to express my gratitude to Dr. Y. Igarashi, who helped me when I started launch operation of MTP and always worked with me in KEK, TRIUMF and J-PARC. I learn a lot from him about hardware and software technique. I am thankful to his kindness and his sense of humor in the working. I would like to express my gratitude to Dr. H. Yamazaki, who helped me with advice when I face problems, and I amazed a his wealth of knowledge about physics. I would like to express my gratitude to Dr. S. Shimizu, who suggested me the strategy of the analysis, and I learned the physicist mind from his passion for physics experiments. I would like to express my gratitude to Dr. K. Horie, who also supported my study, and I admire her clarify statement in the meeting. I would like to express my gratitude to Dr. A. Toyoda, whose one of work of beam test for the development of the aerogel čerenkov counter I had join, and I learned serious attitude as a physicist. I would like to thank to Dr. M. Uchida for his advice operating the MTP. I appreciate the contribution all the TREK collaborators to perform the beam test and support my study. I would like to express my gratitude to predecessor Mr. K. Yoshihara, who suggested me to the importance of learn a lot about detectors and experiments and showed me to this amazing experience. He always give me valuable advice before I entered the graduate school, and helped when I stumbled on a difficulty. I would like to thank all the ICEPP people, staff including CERN in our group, secretaries, elderly students and younger students. Especially, the support from my colleagues, M. Moinaga, R. Kurosaki, K. Owada, T. Inada, W. Choi, I. Otani, T. Yamada, N. Higashi, M. Tani, K. Arima helped me to live the enjoyable studying life. I would like to thank the people and students in the KEK also supported me

to enjoy studying, and encouraged me to write this thesis. I would like to thank the people I met at the TRIUMF and J-PARC also encouraged me to studying. Finally, I deeply appreciate all of my important people, friends and my family for continuous support and encouragement.

# Bibliography

- [1] A. R. Zhitnitkii, *Yad. Fiz* **31**, 1014 (1980).
- [2] V. P. Efrosinin *et al*, *Phys. Lett.* **B493**, 293 (1997).
- [3] F. Sauli, *Principles of operation of multiwire proportional and drift chambers*, CERN, Lectures given in the Academic Training Programme of CERN (1975-1976).
- [4] Particle Data Group, <http://pdg.lbl.gov/>.
- [5] LHC homepage, <http://lhc.web.cern.ch/lhc/>.
- [6] A. Sakharov, in "The Early Universe" by E. W. Kolb and M. S. Turner, *Frontiers in Physics lecture note series* **69** (1989), Addison - Wesley pub.
- [7] KamLAND homepage, <http://www.awa.tohoku.ac.jp/kamland/>.
- [8] G. Luder, *Danske Mat. Fys. Medd.*, *Annals of Physics* **28**, 5 (1957).
- [9] TREK homepage, <http://trek.kek.jp/>.
- [10] M. Abe, *et al.*, *Phys. Rev. D* **072005**, 83 (2006).
- [11] TRIUMF homepage, <http://www.triumf.ca/>.
- [12] J-PARC homepage, <http://j-parc.jp/>.
- [13] S. RIN, *CP violation*, Science co (SGC), 1 edition, 2012.
- [14] K. Kleinknecht, *Uncovering CP Violation : Experimental Clarification in the Neutral K Meson and B Meson Systems*, Springer, 2004.
- [15] CPLEAR homepage, <http://cplear.web.cern.ch/cplear/>.
- [16] Storage Ring Electric Dipole Moment Collaboration homepage, <http://www.bnl.gov/edm/>.
- [17] J.J.Sakurai, *Phys.Rev* **109**, 980 (1957).
- [18] N. Cabibo and A. Maksymowicz, *Phys. Lett.* **9**, 352 (1964).

- [19] S. Eidelman *et al.*[*Particle Data Group*], Phys. Rev. Letters B492. **1**, p.618 (2004).
- [20] M. Kobayashi, T.-T. Lin, and Y. Okada, Prog. Theor. Phys. **95**, 361 (1995).
- [21] G.-H. Wu, K. Kiers and J. N. Ng, Phys. Rev. **D56**, 5413 (1997).
- [22] E. Golowich and G. Valencia, Phys. Rev. **D40**, 112 (1989).
- [23] I. I. Bigi and A. I. Sanda, Phys. Lett. **58**, 1604 (1987).
- [24] R. Garisto and G. Kane, Phys. Rev. **D44**, 2038 (1991).
- [25] G. Bélanger and J. N. Ng, Phys. Rev. **D44**, 2789 (1991).
- [26] Y. Grossman, Int. J. Mod. Phys. **A19**, 907 (2004), ; T Hurth, Rev. Mod. Phys. **75**, 1159 (2003).
- [27] K. Ikado, Talk given at Flavor Physics and CP violation (2006), Vancouver.
- [28] Y. S. Y. Okada and M. Tanaka, arXiv:hep-pf/9704223 .
- [29] G.-H. Wu, K. and J. N. Ng, Phys. Lett. **B392**, 93 (1997).
- [30] M. Fabbrichesi and F. Vissani, Phys. Rev. **D55**, 5334 (1997).
- [31] D. K. Ghosh, X.-G. He, B. H. J. McKeller and J.-Q. Shi, arXiv:hep-ph/0111106 .
- [32] S. Shimizu and K. Horie, TREK Technical Note No.9 Performance of 1/5 prototype chamber studied at KEK FTBL .
- [33] K. Yoshihara, R & D studies of Muon Polarimeter for J-PARC E06 T-Violation Experiment (2011), Master's Thesis, The University of Tokyo.